1998

The role of alloying agents with aluminum for materials compatibility with dilute nitrogen trifluoride plasmas

Brian S. Felker
Lehigh University

Felker, Brian S.

The Role of Alloying Agents with Aluminum for Materials Compatibility with Dilute Nitrogen...

January 11, 1998

The Role of Alloying Agents with Aluminum for Materials Compatibility with Dilute Nitrogen Trifluoride Plasmas

By

Brian S. Felker

A Thesis
Presented to the Graduate and Research Committee
of Lehigh University
in Candidacy for the Degree of
Master of Science

in
Materials Science and Engineering

Lehigh University

December 4, 1997

This thesis is accepted and approved in partial fulfillment of the requirements for the Master of Science.

Dec. 3, 1997
Date

Thesis Advisor
Dr. Kenneth Tarby

Co-Advisor
Dr. Dennis Hess

Committee Member
Dr. John Langan

Committee Member
Dr. David Bohling

Chairperson of Department

ACKNOWLEDGMENTS

To my wife and son, Allyn and Nickolas, without whose undeterred support and understanding this work would still be underway. I will forever appreciate your understanding and unconditional love during the late nights and long weekends, which have finally guided me through to the completion of the difficult task.

I thank Professor Dennis Hess and Professor Kenneth Tarby for the opportunity and privilege of working with them and for their guidance during this process.

I also want to thank Dr. David Bohling, Dr. John Langan, and Dr. Ralph Richardson of Air Products and Chemicals, Inc. for the opportunity to pursue this endeavor and for the use of company resources to complete the research needed for my thesis. Without their support and tutelage this work would not have been as successful. Hopefully you will feel as though this was a worth while experience as well. I want to especially thank Dave and John for inspiring me to set goals and determine a career path and then go achieve them. My life will never be the same thanks to these two fellows.

Furthermore, I want to thank Ed Graddy, Larry Wieserman, TomEvans, and Robert Geoffroy of ALCOA for their manufacturing and donation of the samples and informative discussions about the anodization process of materials.

To Dr. Mark George, Dr. Ron Pearlstein, and Dr. Scott Beck who contributed to this work during many informative discussions and favors, I thank you all.

Jim Stets and Mike Wert provided invaluable help with SEM and EDS measurements and interpretation and sample preparation.

TABLE OF CONTENTS

LIST OF TABLES

LIST OF FIGURES

ABSTRACT

Corrosion has been occurring since man began the practice of metallurgy; attempts at controlling this corrosion have been employed almost as long. In nature, aluminum oxide is more stable and has a lower energy than the metal form. One method of corrosion protection for aluminum metal incorporates an artificially thick oxide layer to reduce the diffusion of reactive species to the base metal. Limiting this diffusion is paramount to having excellent corrosion resistance. This work has compared two alloys of aluminum exposed to NF_3/Ar plasmas at both room temperature and 450 C to determine which alloy has better resistance. By using different alloying agents, the corrosion characteristics of a material can be dramatically altered. In this case, alloy 5352 has a high magnesium concentration while minimizing the silicon and iron concentrations compared to alloy 6061. Alloy 5352 with a surface treatment of unsealed anodization proves to have better corrosion resistance than does alloy 6061. This is due to the interaction of magnesium, with the lack of silicon and iron, with the fluorine. The magnesium forms a protective layer that apparently prevents the fluorine from diffusing toward the base metal beneath.

Currently major PECVD tool manufacturers in the semiconductor industry commonly use hard anodized alloy 6061 for the electrode material. The mechanism of failure of this material is becoming well known. The purpose of this work is to determine the corrosion resistance and mechanism of resistance of a novel alloy. A review of the fundamental electrochemical mechanisms of corrosion, gaseous corrosion mechanisms, and historical perspective of corrosion is given.

1.0 INTRODUCTION

1.1 INTRODUCTION

To date, much of the research that has occurred in the semiconductor industry has been focused on developing the next generation of smaller and faster integrated circuits (IC). Deposition, lithography, etching, polishing, dicing, and packaging are the basic processes used in producing all IC chips. There are over 200 steps needed to produce today's state-of-the-art IC chips. A review of semiconductor processing technology can be found in other sources.[1-5] This study will focus on the material used in manufacturing tools used in plasma enhanced chemical vapor deposition (PECVD).

PECVD processes use a plasma discharge to enhance the deposition of dielectric materials, for example silicon oxide or silicon nitride, that otherwise would need higher temperatures to achieve similar film thicknesses. These high temperatures would increase the diffusion rate of materials already incorporated into the wafer, having a detrimental effect on device performance and yield. Plasma enhancement allows these films to be deposited with good film characteristics while keeping the temperature within an acceptable range. During PECVD processes, material is deposited on the wafer as well as the other exposed interior parts of the reactor. These spurious deposits must be removed after each , or in some cases, several, deposition steps. If allowed to remain on the inner surfaces of the reactor over long periods of time they will eventually grow so thick that they will begin to crack and peel off the chamber walls and drop onto the wafer. These large flakes can cause a variety defects, such as shorts, in the IC chips.[6] This, in turn, lowers device yields and also decreases profitability for device manufacturers.

PECVD reactors are cleaned using one of two methods; a wet chemical clean or a "dry" plasma clean. There are advantages and disadvantages to each cleaning method. For example, wet cleans require that the chambers be opened to the atmosphere and manually scrubbed to remove the deposits. This cleaning method uses solvents which do not chemically attack the exposed parts of the chamber, although, sometimes abrasive scouring pads are used to aid in the removal of the most stubborn deposits.

The advantage of a wet clean over a "dry" clean is that it does not chemically react with exposed parts of the reactor. But this method has several disadvantages including long down times of the equipment, introduction of atmospheric and particulate contamination to the interior of the reactor, and potential exposure of workers to hazardous conditions.

Wet cleans have served the semiconductor industry well for many years, but as the demand for faster circuits, reduced capital expenditures and higher throughputs drive the industry, developing fast and efficient "dry" cleans to meet these demands has received more attention. "Dry" cleans generally use a fluorinated plasma, such as hexafluoroethane (C_2F_6), tetrafluoromethane (CF_4), or nitrogen trifluoride (NF_3), to remove these deposits. Plasma cleans are performed *in situ* and do not require venting the reactor to atmosphere. The down time of the equipment and potential worker exposure is also minimized. These factors impact cycle times for the reactor; i.e., more wafer starts per hour.

Aggressive chemistries are used for these cleaning steps to achieve very fast removal rates of the dielectric material. As a result, the exposed chamber materials can experience some degradation over time, leading to increased costs to maintain the

equipment. Aluminum alloy 6061 is the most commonly used material in the construction of PECVD chambers and internal hardware and is known to degrade over time. Understanding why these parts degrade has become a paramount concern for IC and PECVD reactor manufacturers.

If the mechanism of failure can be identified, then a solution to the problem is more likely to be found. This study investigates two alloys of "hard" anodized aluminum and compares them under similar capacitively coupled rf plasma conditions, a standard configuration in many existing production tools. The particular conditions used in the experimental reactor for this study were chosen to emulate those used in IC production reactors.

In a previous study, a comparison was made between the above mentioned fluorinated plasmas (C_2F_6,CF_4, and NF_3) to determine which had the fastest etch rates under various conditions.[7] Langan and co-workers showed in this study that dilute NF_3/argon plasmas had the fastest etch rate of silicon dioxide and silicon nitride compared to carbon based chemistries. This observation is in contrast to conventional wisdom on etch mixtures and their effect on etch performance. In particular, table 1 shows the three plasma clean recipes and their respective etch rates for the two silicon based materials. It is clearly illustrated that the NF_3/Ar plasma experiment has the fastest etch rates using the smallest amount of fluorinated gas. The conditions for these experiments were 1.4 watts/cm^2 power density, 53 standard cubic centimeters per minute (sccm) total gas flow rate, and 73 pascal.

	Silicon Dioxide (SiO_2) film (Angstroms/minute)	Silicon Nitride (Si_3N_4) film (Angstroms/minute)
25% NF_3 in Ar	670	8000
50% C_2F_6 in O_2	310	4000
92% CF_4 in O_2	130	1800

Table 1: Summary of the etch rates of SiO_2 and Si_3N_4.

Understanding why dilute NF_3 plasmas etch these films faster than the fluorocarbon gases lead to some interesting revelations. Fluorocarbon plasmas are diluted with oxygen to prevent the deposition of teflon, $-CF_2$ polymer, inside the reactor. This chemistry has competing mechanisms of etching and deposition that are controlled by the amount of oxygen in the plasma. Using the ratios identified above for each fluorocarbon gas maximizes the rate of the etch process and minimizes the rate of the deposition process. The main reason why the fluorocarbon plasmas etch at slower rates is that the bond energy, given in table 2, for the first fluorine atom of these molecules is much higher than that of NF_3.

	Bond Energy (kJ/mole)
Nitrogen Trifluoride	247
Tetrafluoromethane	544
Hexafluoroethane	532

Table 2: Fluorine Bond Energies.[8]

Holding all other process variables constant, this says that for a fixed amount of energy input to the plasma, NF_3 will liberate more free fluorine atoms than the fluorocarbons will, solely due to the bond strength of the molecules. Since atomic fluorine is the species that is the active agent in the etch process under conditions relevant to

PECVD chamber cleaning[6], this shows how one fluorine donating gas can produce different etch results compared to another gas.

Based on the previous work, the optimal recipe for this experimental system is 25 mol-% NF_3/Ar at 67 pascal and 1.4 watts/cm^2 rf power density. This work will examine the effects of this recipe on a typical material of construction, sealed hard anodized aluminum alloy 6061 T6 and a novel variant sealed hard anodized aluminum alloy 5352. Bare and unsealed hard anodized aluminum 6061 and 5352 samples are also investigated.

1.2 SCOPE OF THIS WORK

The scope of this work was limited to examining three different surface preparations of the samples; 1) untreated(bare), 2) anodized/unsealed and 3) anodized/hot deionized water sealed. As described above, the plasma conditions were fixed for all experiments and were chosen to emulate the aggressive fluorine containing plasmas used for PECVD chamber cleaning. Two alloys of aluminum were examined, alloy 6061 T6 was chosen because it is a very common alloy used for this application. Alloy 5352 was chosen as it may exhibit superior corrosion resistance due to its different composition. This work was completed in an experimental capacitively coupled rf parallel plate reactor which was designed to roughly emulate the GEC standard reference cell.[9]

2.0 EXPERIMENTAL METHODS AND EQUIPMENT

2.1 SAMPLE MATERIALS

Aluminum pieces that are submerged in an acidic solution and attached to a current source as the anode of the circuit for the purpose of growing an artificially thick oxide layer are said to be anodized. Two competing mechanisms take place at the surface of the aluminum pieces, growth of an oxide layer and dissolution of the oxide layer. There are actually two types of layers that make up the anodized film, a thin barrier layer and the overlying thick pore structures. The barrier layer is very thin, usually about 15-30 nanometers (nm), non-porous, and is of the same form as a natural oxide layer. In the anodization process, it forms first and its thickness is dependent on the voltage applied. The second, outermost layer is microporous and has a columnar structure.[10,11]

Anodized layers can be either classified as "soft" or "hard", the difference between them is the acid solution and electrical settings used and the resulting oxide layer properties. The samples used in this study were hard anodized. Hard anodization (hereafter called anodization) chemistry used a 7% sulfuric acid solution held between -5 and 5 °C. The current density applied was between 2-5 amps per square decimeter and the voltage was in the range of 23-120 volts. These anodized layers can be grown as thick as 250 μm, due the low temperatures, high current densities and slow dissolution of the oxide film in the sulfuric acid. The resulting "hard" anodic coatings have high film hardness and abrasion resistance as their primary characteristics. They are usually thicker than 25 μm and are usually left unsealed, although the pores can be filled to give particular

surface properties.[11] Sealed samples used in this study were sealed by submersion in boiling deionized water (DI). Boiling DI water penetrates the oxide layer pores easily and hydrates the pore walls and underlying barrier layer causing swelling thus filling the pores with aluminum hydroxide. In most cases, sealed anodized layers are more robust because they are impervious to liquids and are more resistant to chemical attack.[11] Wernick et al. also indicate that elevated temperatures can reduce corrosion resistance properties, although they do not state the mechanism for this reduction.

Samples used in this study were aluminum alloy 6061 T6 and aluminum alloy 5352 supplied by Aluminum Company of America (ALCOA). The sample dimensions were 2.540 cm diameter disks, 0.635 cm thick, with 0.159 cm radius edges. The surface finish of the sample before anodization was between 1.270 μm and 2.032 μm. The anodized samples had a surface finish between 2.032 μm and 3.048 μm. The samples were hard anodized using typical methods commonly used in industrial applications. The anodized layers of the samples used were 50.0 μm +/- 5μm in thickness. The samples were stored in a nitrogen purged box until use.

Each aluminum alloy had three types of surface preparation; untreated (bare), anodized/unsealed, and anodized/sealed. All bare metal samples were chemically cleaned using isopropyl alcohol after machining to remove any oils. Anodized/unsealed samples were anodized using the above method while the anodized/sealed samples were both anodized/sealed using a boiling deionized water bath in which the samples were submerged.

2.2 XPS SYSTEM

Representative samples of each type were examined using X-Ray Photoelectron Spectrometry (XPS) depth profiling to determine their "as received" elemental chemical concentration as a function of depth. A Perkin-Elmer double pass cylindrical mirror analyzer (CMA) surface analytical system was used to complete the depth profiles. The Perkin-Elmer system has a dual anode x-ray source (model no. 04-548) having both magnesium and aluminum K_α x-rays. The energy of the magnesium and aluminum x-rays are 1253.6 and 1486.6 electron volts (eV), respectively. These x-rays penetrate the surface of the sample between 1-10 μm.

A differentially pumped argon ion sputter gun (model no. 04-303) was internally rastered across the sample surface in a 3.33 mm x 4.67 mm square pattern. This pattern was chosen to avoid edge effects from the crater while depth profiling. The ion beam was used at an energy of 5 keV and it's sputter rate was calibrated using three different thin films; silicon dioxide on silicon, tantalum oxide on tantalum, and aluminum oxide on silicon.[12] The calibration curves are shown in figures 2.1-2.3.

The XPS data acquisition is controlled by a computer program supplied by Physical Electronics, formerly Perkin-Elmer, called PC Explorer version 3.4. This software communicates with a computer board (model 137) and uses TTL links to control the x-ray source and the argon ion sputter gun.

The binding energy scale linearity of the CMA was calibrated by examining copper and gold samples that were sputtered clean of oxygen and carbon contamination. The copper $2p_{3/2}$ peak positioned 932.4 eV and the gold $4f_{7/2}$ peak positioned at 83.8 eV for

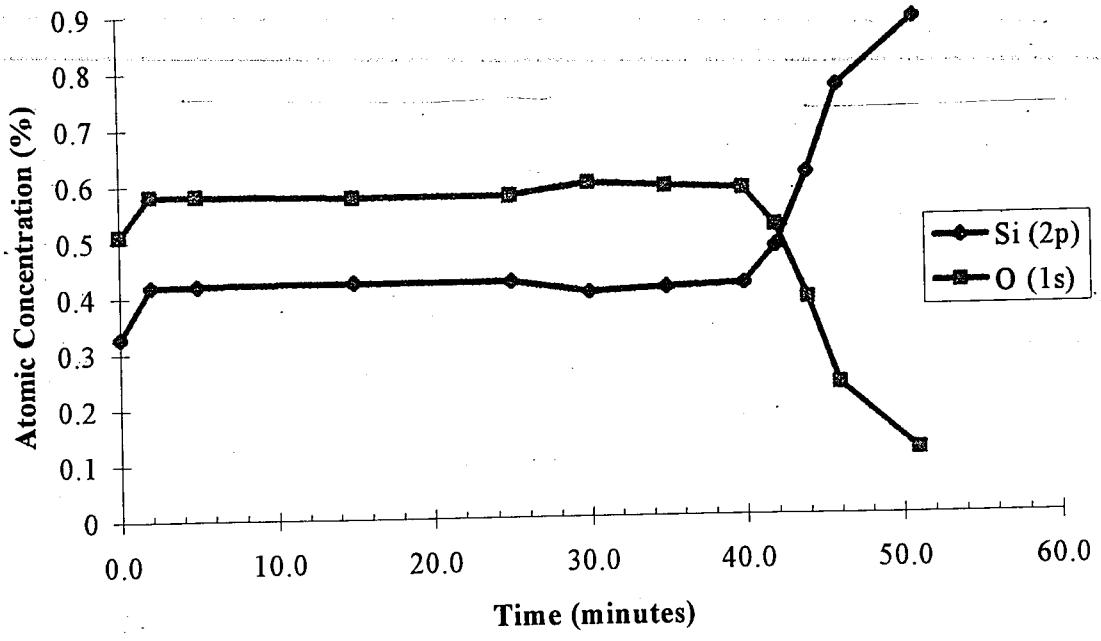

Figure 2.1: Silicon dioxide sputter calibration at 5keV beam energy. Film thickness is 500 Å and the SiO_2/Si interface is reached in 45 minutes yielding a sputter rate of 11.1 Å/min.

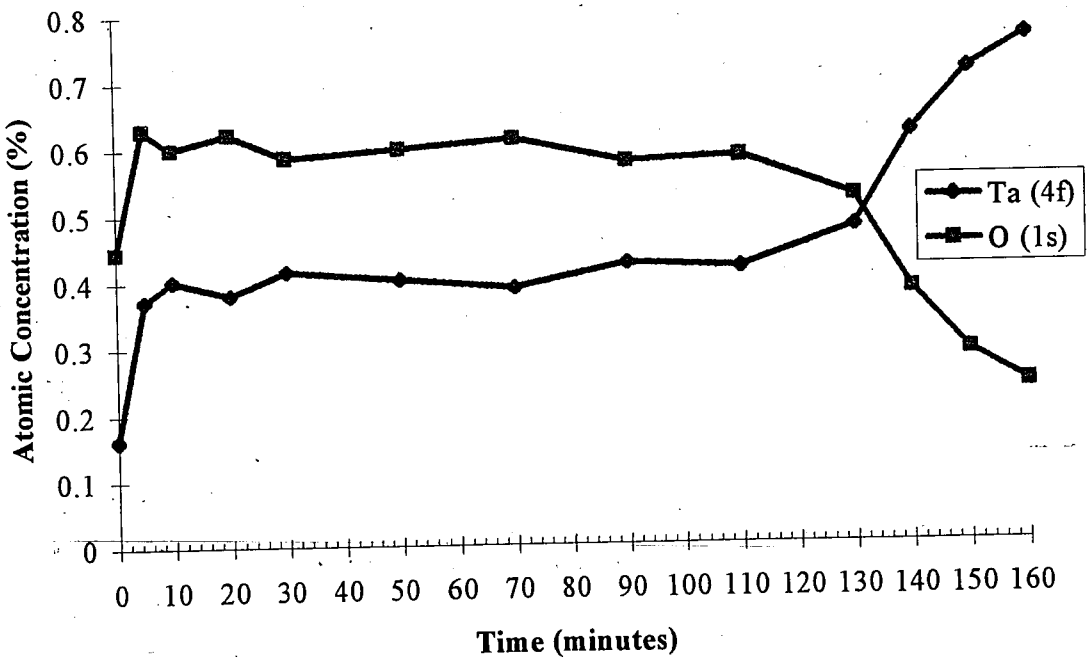

Figure 2.2: Tantalum Oxide sputter calibration at 4 keV beam energy. Film thickness is 1000 Å and the Ta_2O_5/Ta interface is reached in 132 minutes yielding a sputter rate of 7.6 Å/min.

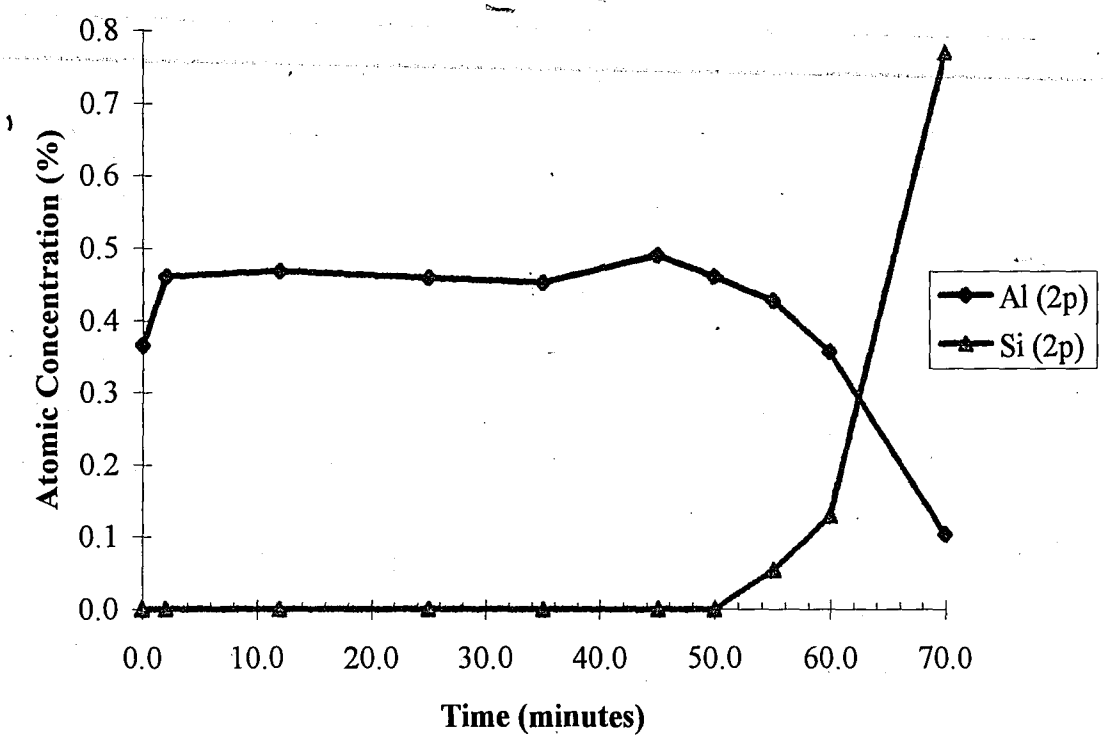

Figure 2.3: Aluminum Oxide sputter calibration at 5 keV beam energy. Film thickness is 514 Å and the Al/Si interface is reached in 62 minutes yielding a sputter rate of 8.3 Å/min.

reference points were used to calibrate the spectrometer for magnitude and linearity of the binding energy scale. The work function for our spectrometer was determined to be 3.60 eV. The general survey data, covering a complete scan of accessible binding energies, was collected by the tool at a pass energy of 100 eV at a resolution of 1 eV/step. While using magnesium x-rays, the binding energy ranged from 1100 eV to zero eV and the range used for aluminum x-rays was 1350 eV to zero eV. All survey spectra were averaged over 10 scans. The higher resolution, or multiplex, scans over specific energy regions were taken at 25 eV pass energy with a resolution of 0.25 eV/step. All multiplex region spectra were averaged over 20 scans. The specific regions examined are listed in table 1 with the binding energy ranges.

Element	Peak Electron Orbital	Binding Energy Range (eV)	Atomic Sensitivity Factor
Aluminum	2p	86-66	0.11
Oxygen	1s	542-522	0.63
Fluorine	1s	695-675	1.00
Magnesium	1s	1320-1300	3.65
	2p	60-40	0.07
Carbon	1s	294-274	0.21
Silicon	2p	114-94	0.17
Sulfur	2p	173-153	0.35

Table 1: Multiplex regions with the corresponding electron orbital, binding energy range and atomic sensitivity factors.[13]

For all XPS spectra there were 15 kilovolts and 300 watts applied to the x-ray source. The emission current for the ion gun filament was set to 25 milliamps and the argon pressure inside the ion gun was regulated by a Granville-Phillips leak valve at a pressure of 15 millipascal during sputtering. The computer software switches the ion gun and x-rays on and off automatically. The sputter intervals, unless otherwise stated, were five minutes in length. After each sputter interval, the ion beam was turned off, the x-rays were turned on, and the multiplex data collected, constituting a cycle of the depth profile. From the sputter rate calibration data, the depth into the layer was determined. After each sample was exposed to the plasma, it was then moved into the XPS analysis chamber *in vacuo* with the use of magnetically coupled transfer arms and sputter depth profiled.

The base pressure of the XPS chamber was $1.33(10)^{-8}$ pascal, during spectral acquisition it was $6.66(10)^{-7}$ pascal, and during sputtering it was $6.66(10)^{-6}$ pascal. The sample transfer time was less than 10 minutes from the plasma reactor to the XPS chamber and the pressure during the transfer was $1.33(10)^{-5}$ pascal or lower.

2.3 PLASMA PROCESSING SYSTEM

The plasma chamber used for the sample exposure was constructed from 304 stainless steel. The main chamber is 30.48 cm in diameter and 15.24 cm high. There are eight ports around the perimeter of the chamber, as seen in figure 2.4. The gas is delivered to the chamber through port #2 by 316 stainless steel tubing regulated by MKS mass flow controllers (MFC) (model nos. 1159 and 2159). The inlet pressure of the MFC is 125 kPa which is regulated down from the cylinder pressure. The gas flow is parallel to the electrode surface. The gas is exhausted from the chamber 180 ° from the entrance point by an Alcatel molecular drag pump (model no. 5030CP) and a mechanical backing pump (model no. 2004). Chamber exhaust is diluted with nitrogen, and fed to a series of active fluoride scrubbers before being vented to the house exhaust system. Two ports, located 180 ° apart, has gate valves which isolate the chamber from the magnetic transfer arm and the sample introduction load lock. There is one quick access hatch that measures 15.24 cm in diameter. The remaining ports are quartz viewports. The base pressure of the reactor is $6.66(10)^{-5}$ pascal.

The plasma system consists of two horizontal electrodes, that are 7.62 cm in diameter, with an interelectrode gap spacing of 2.54 cm. The upper electrode is powered by an RF Power Products 1000 watt rf power supply operating at 13.65MHz (model no. RF-10). The power supply is connected to a Bird in-line watt meter (model no. 43) by RG-213 coaxial cable. The watt meter is coupled to an RF Power Products "L"-type matching network (model no. AM-10), which in turn is coupled to the upper electrode.

The lower electrode is grounded to the chamber. The lower electrode contains a

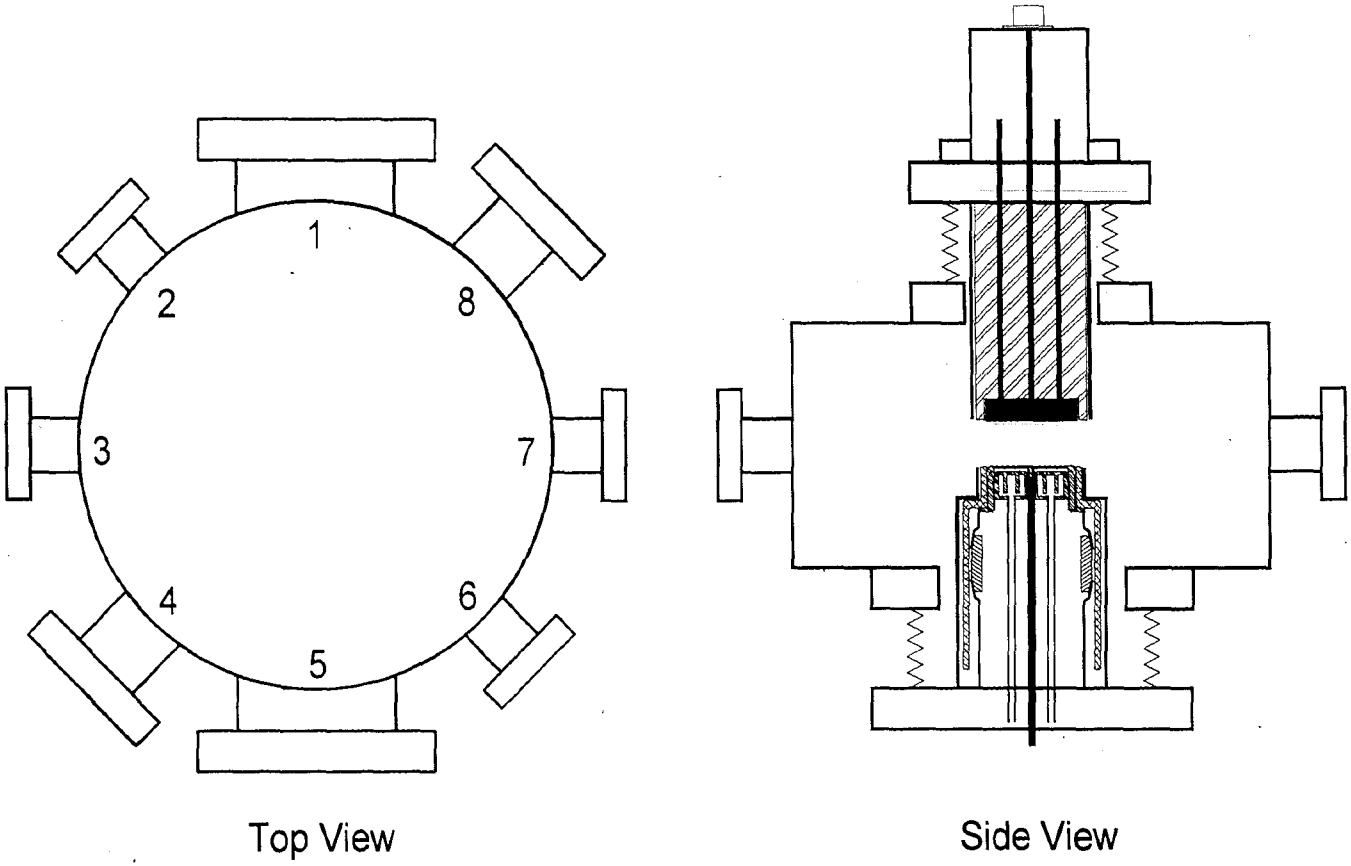

Figure 2.4: A top and side view of the plasma reactor. The ports descriptions, labeled on the top view, are 1) Viewport, 2) gas inlet, 3) gate valve to the sample load lock, 4) viewport, 5) solid quick access door (no viewport), 6) gas exhaust and chamber pressure, measurement point, 7) gate valve to the magnetically coupled transfer arm, 8) viewport

heater element to heat the samples to ~450 °C, see figure 2.5. The heater element consists of graphite encased in electrically insulating boron nitride. An Omega PID temperature controller (model no. 6100) regulates 120 a.c. volts to the heater element. Oxygen free high conductance (OFHC) copper rods, 0.318 cm in diameter, screw directly into the heating element for minimal contact resistance. Temperature is sensed at the atmospheric side of the electrode surface by two K-type thermocouples. One thermocouple is for the PID controller and the second is for an independent over temperature alarm circuit. The calibration for the heater set point versus the sample surface temperature can be seen in figure 2.6. Set point temperature was measured using the PID thermocouple located at the atmospheric side of the electrode. Sample surface temperature was measured using a second type K thermocouple inserted into the reactor through vacuum feedthrough in port #8 and resting on the sample surface. The temperatures were recorded by a Rustrak Ranger data storage unit every 10 seconds.

The heater element is insulated from a cooling jacket by a 0.635 cm thick piece of mica. Mica is both thermally and electrically insulating. A cooling jacket removes any stray thermal energy that does not contribute to heating the sample. Ethylene glycol is circulated from a Haake chiller/recirculator (model no. F3) through the aluminum cooling jacket. Deionized water is circulated through the upper electrode and chilled to 20 °C by a Neslab chiller/recirculator (model no. CFT-25).

The electrode shell is composed of several pieces, as seen in figure 2.5. The electrode surface is made of nickel and is welded to a 304 stainless steel side wall, in which the cooling jacket and heater element are housed. This side wall attaches to a

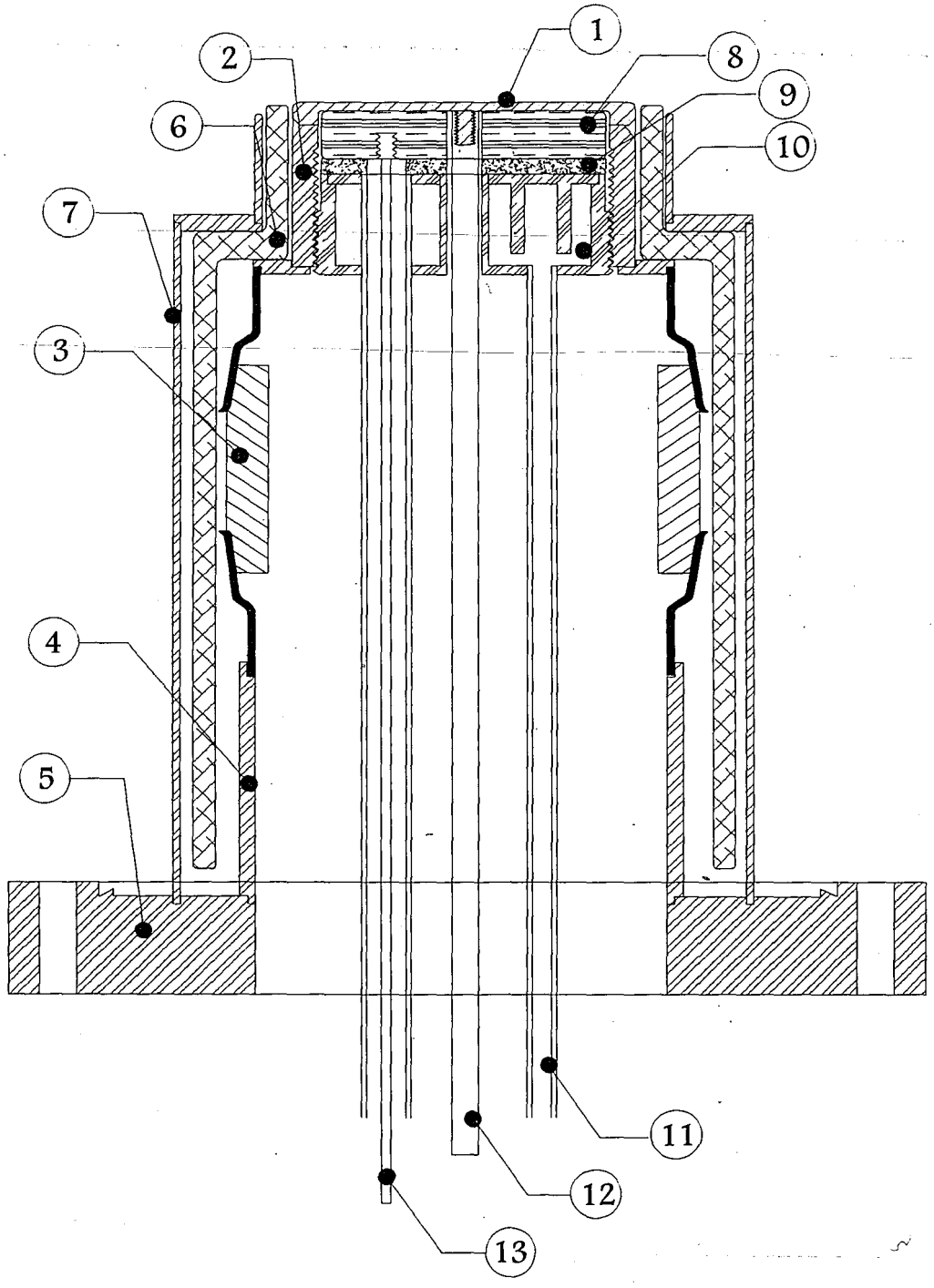

Figure 2.5: The lower electrode assembly: 1) nickel top plate, 2) 304 SS side wall, 3) ceramic break, 4) 304 SS extender ring, 5) 304 SS conflat base flange, 6) boron nitride ceramic insulator, 7) 304 SS ground shield, 8) boron nitride coated graphite heater element, 9) mica insulator, 10) aluminum cooling jacket, 11) aluminum cooling line, 12) OFHC copper rod to electrode, 13) OFHC copper rod to heater.

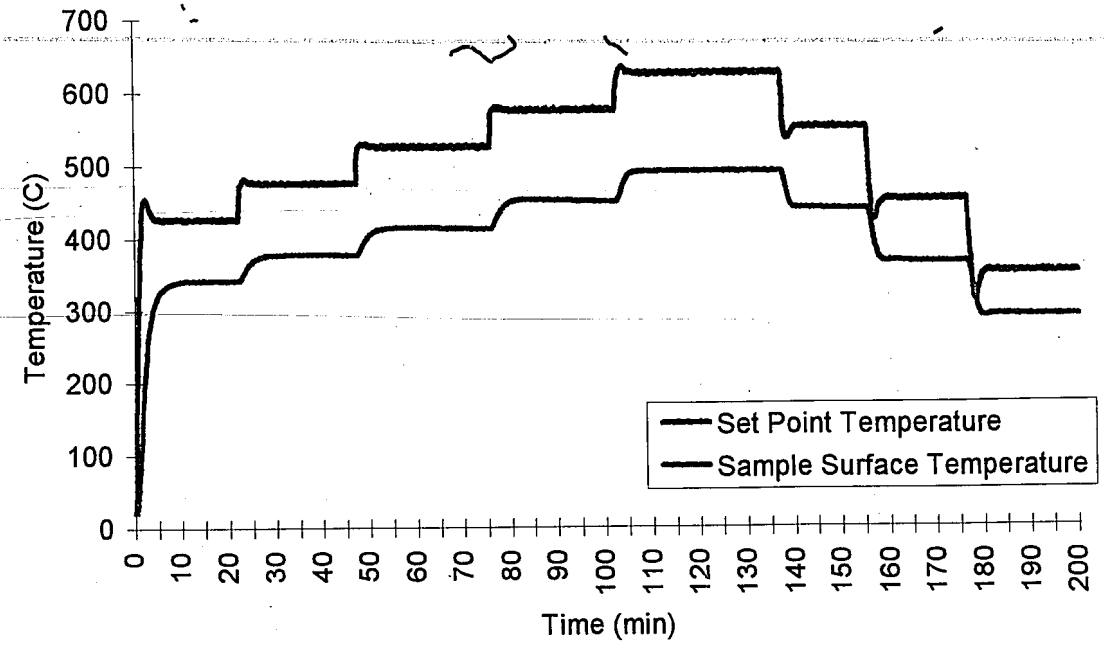

Figure 2.6: Heater calibration curve between sample surface temperature and the set point temperature. The sample was aluminum alloy 6061.

cryogenic electrical ceramic break which electrically and thermally isolates the electrode surface from the remainder of the chamber. The electrode is grounded to the chamber via a 0.635 cm diameter OFHC copper rod that threads onto the back side of the nickel top plate and a short length of silver coated copper braid. The lower electrode surface is electrically isolated from the chamber to provide the capability of powering the lower electrode either with rf or dc power in other experiments.

The lower electrode assembly is mounted on a McAllister Technical Services z-axis stepper motor controller (model no. BLTM-86XS-3) that allows reproducible electrode height after loading and removing samples from the chamber. Samples are loaded into a load lock and a magnetic transfer arm is used to retrieve and place the

samples onto the lower electrode. After the samples are loaded onto the electrode and the electrode is returned to the proper process position, the samples are exposed to a 25% nitrogen trifluoride (NF_3) in argon (Ar) plasma under the following conditions: 50.66 k Pa, 12.5 sccm NF_3, 37.5 sccm Ar, 60 watts, for 60 minutes. After exposure, the samples are transferred *in vacuo* to the XPS analysis chamber for surface analysis and sputter depth profiling. Figure 2.7 shows a schematic of the experimental apparatus.

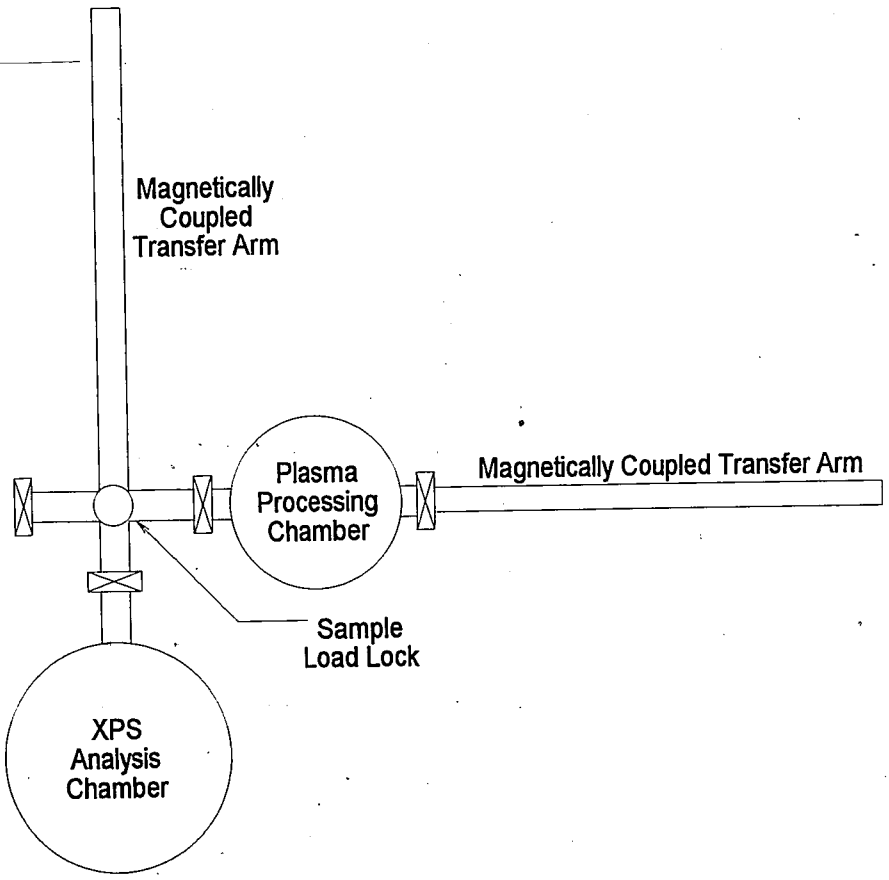

Figure 2.7: An top view of the XPS/Plasma cluster tool. This enables *in vacuo* transfers of the samples between the processing and surface analysis chambers.

Figure 2.8 is a photograph of a sample resting on the lower electrode during an NF_3/Ar plasma exposure. The sample is resting in the center of the lower electrode. The brightness of the plasma can be correlated to the plasma density in a qualitative way by stating the brighter the glow the more dense the plasma. Sheath areas are visible for both electrodes. While the sample does substantially perturb both sheath regions, this fact does not detract from the information gained from this study.

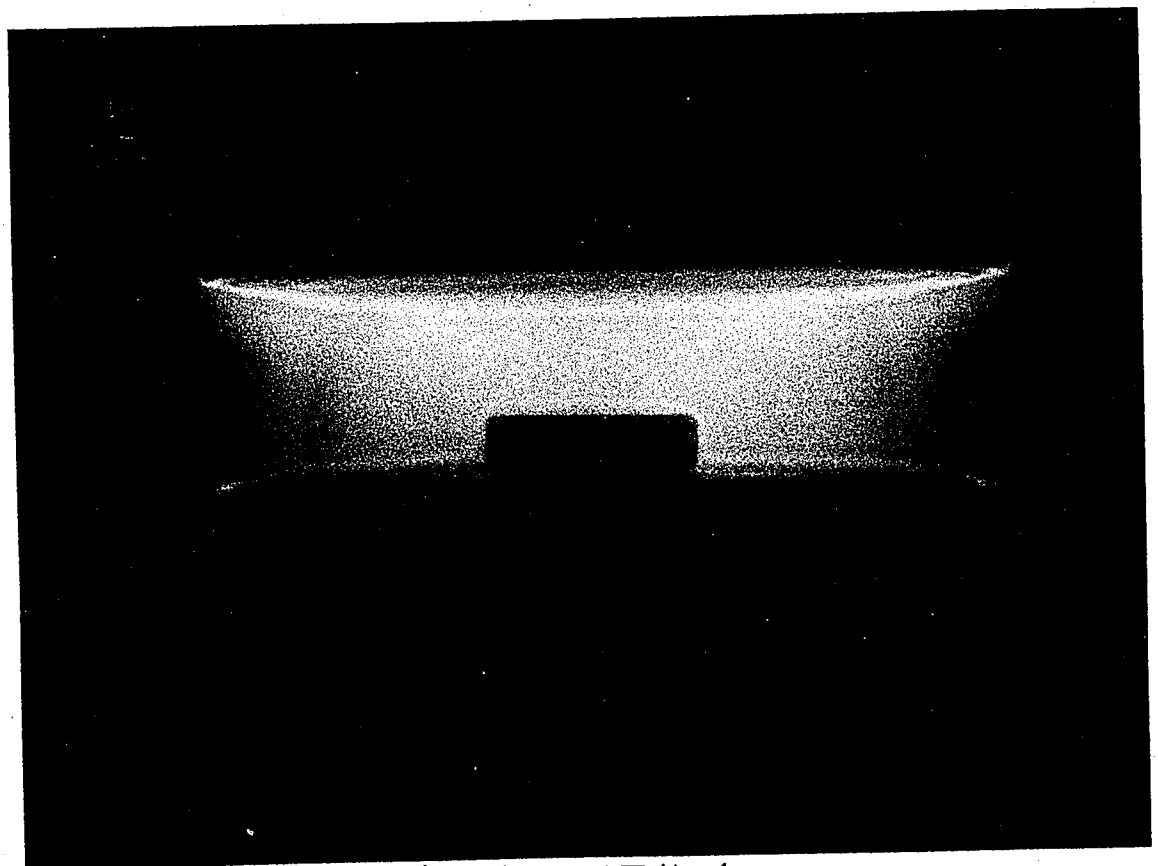

Figure 2.8: Photograph of a sample during an NF_3/Ar plasma exposure.

Figure 2.8 is a photograph of a sample resting on the lower electrode during an NF_3/Ar plasma exposure. The sample is resting in the center of the lower electrode. The brightness of the plasma can be correlated to the plasma density in a qualitative way by stating the brighter the glow the more dense the plasma. Sheath areas are visible for both electrodes. While the sample does substantially perturb both sheath regions, this fact does not detract from the information gained from this study.

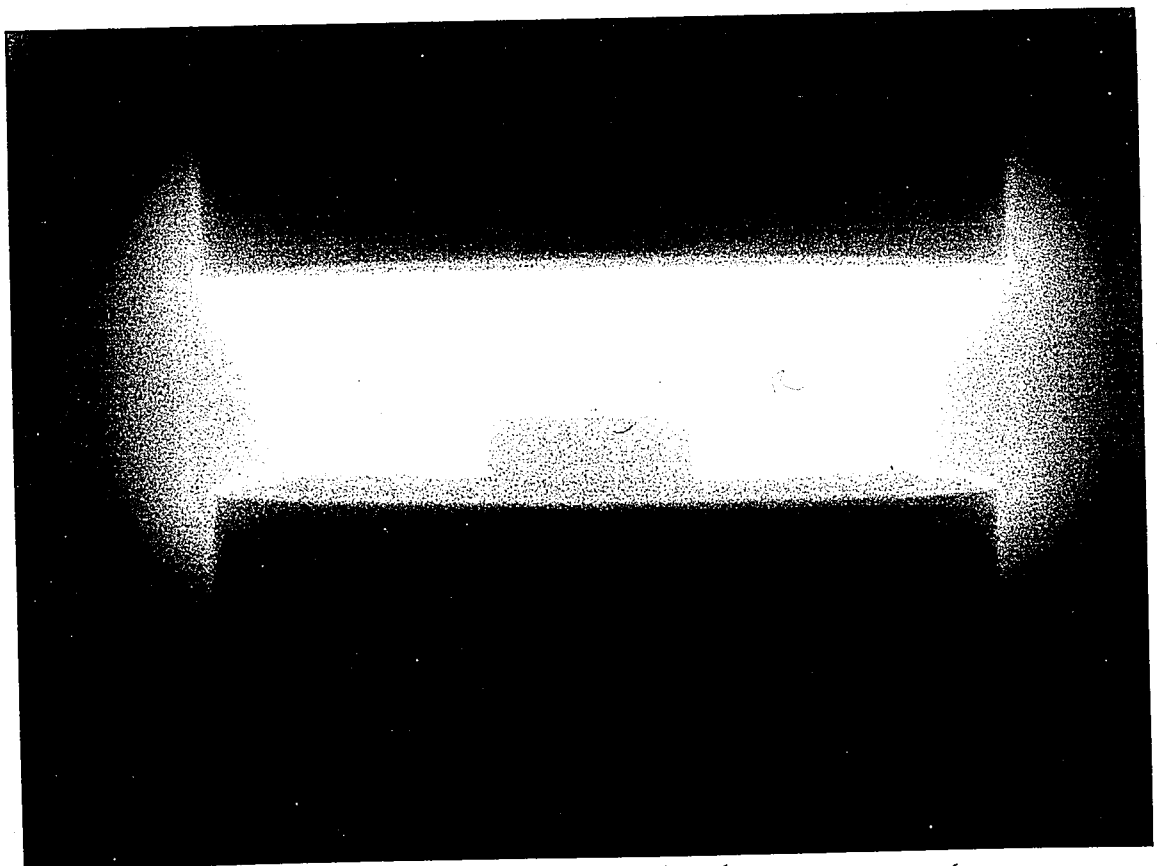

Figure 2.8: Photograph of a sample during an NF_3/Ar plasma exposure.

2.4 SEM AND EDS SYSTEM

A Joel scanning electron microscope (SEM) (model no. JSM-840A) with a Noran energy dispersive spectrometer (EDS) (model no. Voyager 3) was used to collect cross sectional images and atomic concentration data of the hard anodized layer of the samples. Samples were examined "as received" and following plasma exposure. As received samples were mounted in an organic binding material, polished, and examined. Post plasma exposure samples were cut using a diamond saw and mounted in a spring jaw holder for analysis. Since polymer mounting and polishing could disturb the elemental composition of the plasma treated samples, they were not used for the exposed samples. EDS analysis was performed on a region where the saw did not contact the anodized layer. A region was chosen where the saw blade ripped material away and left a slight recess from the cross sectional surface. By choosing a region in this manner, the EDS measurements yielded fluorine concentration values in the anodized layer that are consistent with those trends observed using XPS analysis.

All samples examined by SEM were sputter coated with a thin gold-palladium layer (50 Å) to reduce charging in the anodization layer. The reported EDS intensities were then ZAF corrected. This procedure used the atomic number, absorption, and fluorescence characteristics of the elements detected to normalize for analyzer sensitivities and probability of detection. Standards (aluminum oxide powder, calcium fluoride and elemental sulfur powder) were used for the various elements to determine the ZAF corrections. SEM analysis for the "as received" samples used an electron beam voltage of 15 KeV while the post plasma exposure samples used an electron beam voltage of 5 KeV.

The lower voltage was used to improve the oxygen and fluorine sensitivity. Ten points across the anodized layer and into the bulk were acquired, approximately 8 microns apart. Several closely spaced points were acquired near the interface.

Additional error, possibly as much as 10 %-15 %, may have been introduced into the EDS intensities[14] by not polishing the plasma exposed sample surfaces and by depositing a thin gold-palladium coating to reduce charging. Bastin and Heijligers do not specifically indicate that there is error associated with the use of a gold-palladium coating; however, the information discussed does heighten awareness to the issue. Gold and palladium x-ray energies that were detected do not overlap any of the x-ray energies of the elements used for this analysis, so the gold and palladium signals did not affect data interpretation. The plasma exposed sample EDS analysis should only be used qualitatively due to the additional uncertainty of the roughened surface and the deposited coating.

3.0 BACKGROUND

3.1 A BRIEF HISTORY OF CORROSION

Ever since man began practicing metallurgy, metals have experienced corrosion. From that time until now, man continues to explore different methods of slowing this inevitable process. Pliny, a great Roman philosopher, wrote at great length about *ferrum corrumpitor*, or 'spoiled iron'.[15] In this work he asks himself a most difficult question, "Why iron should corrode more easily than other metals?". Because the experimental techniques of later years were not available to him, he arrived at a metaphysical solution- "because iron is both the best and the worst of man's servants."

The oxide form of most metals has a lower total free energy than the pure metallic form. War has long since been the driving force of increasing knowledge of materials properties. Attempts to prevent the corrosion of metallic weapons and armor lead to gilding techniques which use heat treatments to create a protective oxide layer on the surface, not to mention an improved appearance of the metal.[16]

The British navy had many reports of bi-metallic corrosion which lead to the failure of metallic components submerged in salty sea water. In 1763, a report was filed with the British Naval Admiralty detailing one of the earliest practical solutions for bi-metallic corrosion. It was noticed that some less corroded iron nails, used to hold copper sheathing in place, had brown paper between the nail and copper. But as with many new ideas of its day, it was mostly disregarded.[17] Atmospheric and aqueous corrosion of metals have created many problems for society and have led to enormous amounts of research

trying to find solutions to this problem. Many industries are affected by corrosion; nuclear, fossil fuel, aerospace, defense, marine and offshore, automotive, construction, electrical, biomedical, chemical and electronics industries to name a few.

Communication of experimental results prior to 1900, are very sparse. Around the turn of the 19th century most corrosion research was focused on the relative corrosion rates of wrought iron, cast iron, and steel. In November 1901, the first meeting of the American Electrochemical Society was held in Philadelphia. The intent of this meeting was to create a structured environment for discussions about experimental results and future electrochemical research.[18] During this time period many influential breakthroughs occurred. Whitney[19] in 1903 demonstrated the electrochemical nature of corrosion and in 1907 Walker showed that the corrosion reaction is sustained by the depolarization of the cathode. Walker and co-workers[20] outlined the controlling factor for the rate and distribution of corrosion.

Williams[21] and Buck[22] determined that the addition of a small amount of copper to low carbon steel dramatically improves the corrosion resistance of the material. Extensive research through the 1920's and 1930's highlighted the importance and influence the material's environment has in controlling the rate of corrosion. By this time researchers were noticing differences in corrosion rates for similar materials in differing environments, such as ambient air, water, sea water, acidic/alkaline solutions, or underground.

During this same time period, protective layers for metals were being examined. The first to gain industrial use was cladding. Cladding rolls, explosion welds or builds up a welded coat of a more corrosion resistant metal onto an exposed surface of a structural

metal to improve the overall corrosion resistance. Combinations, such as nickel on steel, chromium- nickel clad steel, cupro-nickel clad steel, and aluminum on various metals, were first to appear on the open market.

These events lead to the belief that all ordinary steels can be made more corrosion resistant if they were protected by other metallurgical means.[23] What followed were many studies of how to prevent corrosion via coatings and treatments of the material that proved to be economically sound and applicable to many industries. The preference of the time period was to select preventative measures that seem best suited for each specific case. The inhibiting effect and cost spread over the expected or useful life of the metal was compared with the cost of repairs and replacement and loss due to reduction in service capacity during the life of the system. Prevention of corrosion is better than remediation because prevention is better when applied before the trouble is in advanced stages.

In the time period spanning 1900 to the mid-1950's many fundamental advances were made in corrosion science. It was this period that defined corrosion as a science and began the understanding of fundamental electrochemical corrosion. Several organizations were formed worldwide to further the understanding of corrosion phenomena. The fundamental mechanisms of aqueous corrosion, the use of alloying agents to control or enhance corrosion resistance, and the use of cladding or inhibitors to thwart corrosion were just a few of the significant breakthroughs of this era. An exhaustive history of corrosion cannot be presented here due to the shear volume of work in this area, so the remaining focus will be on the results pertaining to aluminum and halogen corrosion.

McKee and Brown[24] reported in 1947 that the corrosion rate of aluminum in solution was dependent on the solubility of the corrosion products in the environment. Metals that have high solubility corrosion products will exhibit poor corrosion resistance. Conversely, corrosion products that have low or no solubility form 'self-healing' protective barriers, thereby stopping or severely limiting the contact of the solution with the underlying base metal.

Penetrating power of the anions through the oxidized layer of aluminum are, in decreasing order chloride, bromide, iodide, fluoride, sulfate, nitrate, and phosphate. Small anions like chloride, bromide, and iodide show high rates of penetration; the fluoride anion, which probably forms a complex ion, has a lower rate of penetration while the sulfate, nitrate and phosphate anions are the slowest.[24]

Aziz and Godard[25] demonstrated that the iron content in aluminum had a marked influence on it's pitting susceptibility. Pitting corrosion of aluminum is controlled by the presence of iron-rich precipitate particles, probably $FeAl_3$, which acts as the cathode for localized cells on the surface.[26] In 1965, Beard and Hine[27] established that different alloying constituents affect the corrosion resistance properties of aluminum in a mercury environment. This follows from the initial work done with iron in the earlier part of the century where copper additions were used to improve corrosion resistance.

Olden and Cameron[28] highlighted how society's demand for better products that are longer lasting and cheaper to purchase drive industry to change the way things have been produced toward new more efficient processes. These authors describe the need to develop cleaner and more efficient processes to produce hydrocarbon gases by converting

liquid reactants into a gaseous product via a high temperature catalysis process. Corrosion of the reaction equipment for this new process was very different than for the old low temperature method.

Extensive research has been completed concerning the corrosion of metals under halogen gas corrosion conditions for the nuclear industry. The nuclear industry, in the late 1950's through the early 1970's, needed materials compatibility information for the design of nuclear reactors and uranium enrichment processes. Compounds like uranium hexafluoride, hydrogen fluoride, chlorine trifluoride and molecular fluorine were tested under many conditions with many materials to determine whether any of the materials could be used in this harsh service.

Vincent and his co-workers investigated[29-31] the gas-solid reactions that can occur during corrosion using four different gaseous species, molecular fluorine, hydrogen fluoride, chlorine trifluoride and uranium hexafluoride. It was determined that the extent of corrosion depended on the interfacial reaction product layer, i.e., the protective layer formed during the exposure. Results ranging from very little corrosion to violent reaction with the substrate were found. Materials that were exposed to these environments included copper, iron, nickel, zinc, cadmium, tungsten, molybdenum, niobium, and silicon. They also examined the liquid-solid reactions using available data for support. It seems that for the case of dilute HF solutions, the more dilute the solution, the more corrosion increases; they speculate that this is due to the ionic nature of the solution. Additional articles examine the effects of anhydrous gaseous environments where the corrosion products were solid, thereby forming a passivation layer. The findings indicate that

pressure has little effect on corrosion, while mechanical stresses can erode the protective layer and thus permit further corrosion.

Metallization schemes used in ICs to make electrical connections to the devices on the chip typically invoke aluminum metal. The designers use aluminum because it has very good electrical characteristics and it forms a thin protective oxide layer to inhibit corrosion. At the high temperatures experienced during heat treating, above about 450C, neighboring silicon is soluble in aluminum and diffuses into the aluminum which causes pitting in the silicon. Rapid thermal annealing steps and diffusion barriers significantly reduce pitting.[4]

There are many more examples that describe specific results for materials used for different applications. In the semiconductor industry, there has been markedly less published about the corrosion resistance properties of the materials of construction of process tools. However, one account by Langan and Felker[32] describe how fluorine incorporation into the anodization layer of alloy 6061 using different fluorine containing source gas plasmas can lead to extensive damage of the aluminum part.

Ponnekanti et al.[33] describe how different alloy constituents can lead to longer useable lifetimes of the aluminum parts in PECVD tool use. They cite the primary failure mechanism in these parts as the formation and growth of aluminum trifluoride (AlF_3) under the anodization layer eventually growing large enough to flake off the protective layer exposing the underlying metal.

3.2 FORMS OF CORROSION

Corrosion can be defined as the degradation of a metal by an electrochemical reaction with its environment.[17] Dissecting this definition tells us that corrosion is an undesirable process that leads to electron transfer with the surrounding solution, which can be influenced by electrical potentials. There are several different mechanisms of corrosion such as pitting, intergranular, crevice and poultice, galvanic, exfoliation, stress and fatigue.[11] Figure 3.1 provides a schematic view of each type of corrosion.

Uniform corrosion removes metal from the surface unilaterally as a result of the environment having access to all surfaces of the material and the material being compositionally uniform. Atmospheric corrosion is the best example of this type of corrosion. Galvanic corrosion occurs when two dissimilar metals are coupled together and one of the metals has a markedly lower electrochemical potential than the other metal. The lower potential metal will be preferentially corroded.

Crevices between two surfaces, such as the space between a washer and bolt, tend to exhibit faster corrosion than the openly exposed surfaces. If there are different materials involved, galvanic corrosion may also play a role. Localized attack on an otherwise protected surface is called pitting corrosion. Pits can have many different shapes, but deep pits could lead to wall penetration and leaking.[34]

Environmentally induced cracking (EIC) is earmarked by unusually brittle characteristics from a normally ductile material. EIC can be found in three related forms: stress corrosion, corrosion fatigue and hydrogen embrittlement. Stress corrosion and corrosion fatigue cracking are a result of stresses placed on a material over time. The

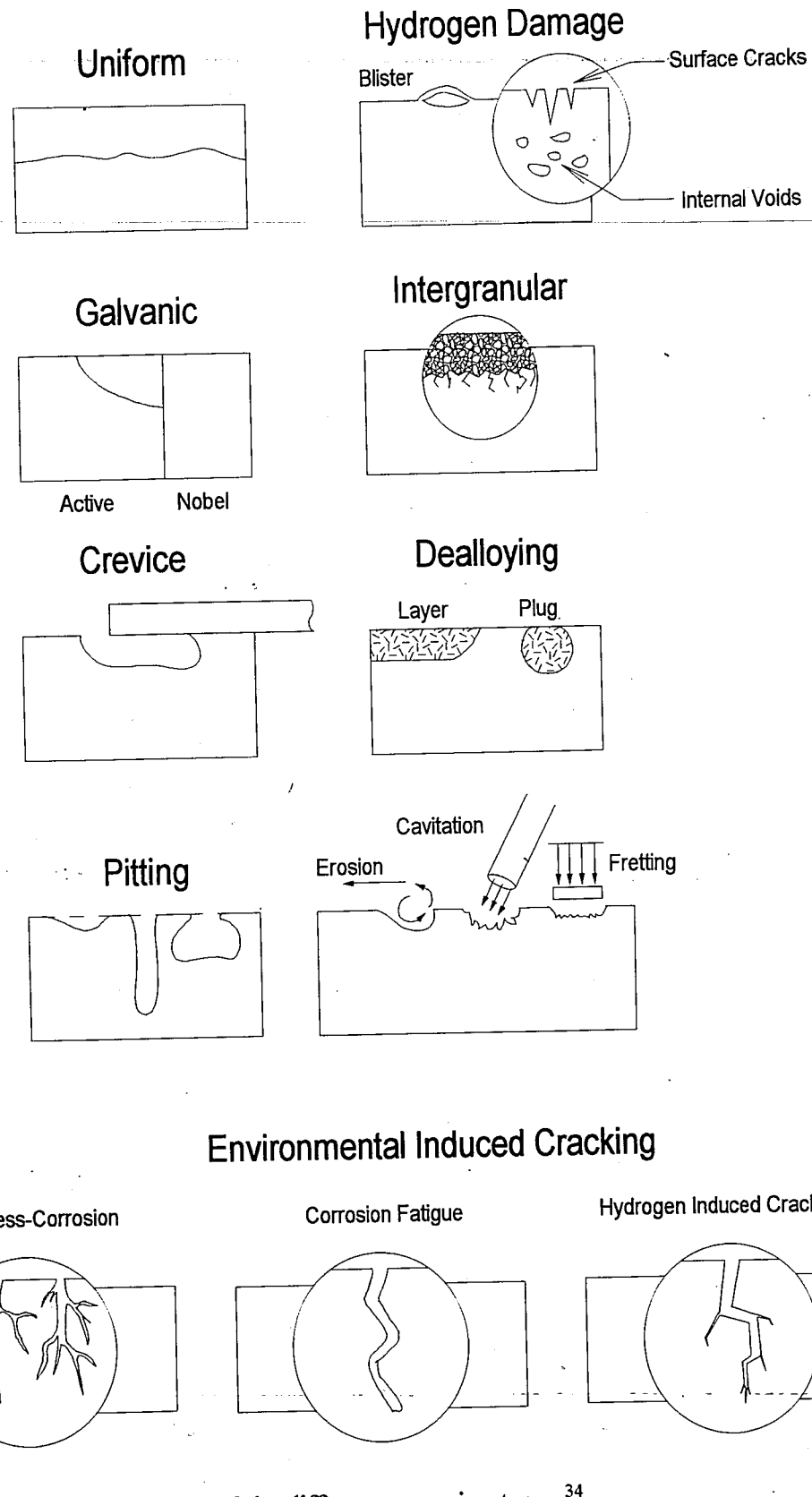

Figure 3.1: Schematic view of the different corrosion types.[34]

combination of the stresses and the environment create cracks in the materials. Stress corrosion typically has static stresses while corrosion fatigue stresses are cyclic.

Hydrogen embrittlement results from large amounts of molecular hydrogen diffusing into the material lattice and, upon heating, creating blisters, voids, decarburization, or methane production in carbon steels. Atomic hydrogen can be produced at the metallic surface during several surface processes, such as electroplating or pickling. Hydrogen incorporation at lower levels can be reversed by driving the hydrogen out of the material with high temperature baking. Higher levels of hydrogen will lead to further damage, such as blisters, voids, cracks, and hydride formation. Hydrogen cracks are less branched than stress corrosion cracks.[33-35]

Most materials are not 100% pure and have either low level impurities or alloying elements that can provide beneficial characteristics to the material. These impurities can diffuse to the surface and help passivate the material or segregate, thus leaving areas of depletion or vulnerability behind; for example, grain boundaries. Grain boundaries are already a prime target for corrosion to occur providing both higher energy levels and diffusion pathways farther into the material. This is called intergranular corrosion.

Some alloy constituents have lower electrochemical potentials than the others and will dealloy to corrode preferentially. Brass is especially susceptible to this type of corrosion due to the lower electrochemical potential of zinc.

Systems that transport reactive fluids often exhibit erosion corrosion. The corrosivity and velocity of the fluid remove material from the wall and subsequently weaken the part. Any particles that may be carried along in the flow will only serve to

enhance this type of corrosion. In systems with very high fluid velocities cavitation can occur. Cavitation occurs in fast flow systems which create pressure reductions that can condense out water droplets which then implode on the wall material creating local pressure bursts. These pressure bursts can damage any protective film that resides on the material surface or even dislodge particles, thus creating giant pathways to the base material for corrosion to continue. Fretting is the vapor phase analog of cavitation. Repeated movement of the corroding material and another solid under load causes abrasions of the oxide coating, which eventually exposes the underlying base material. There are particles created within the system which further promote corrosion downstream.[17,34,35]

There are many pathways to destruction resulting from corrosion. All the above phenomena have many things in common. Most important of these similarities is thermodynamics. What follows is a fundamental discussion of classical electrochemical corrosion. Once basic corrosion mechanisms are discussed the influence of corrosion in materials compatibility will be examined.

3.3 THERMODYNAMICS OF CORROSION

In general, corrosion reactions are governed by the following general reaction equation:

$$A + B = C + D \qquad \text{Eq. 1}$$

where A and B are reactants and C and D are reaction products.[17] If material A is a metal, then in this reaction it gives up electrons and becomes oxidized. The driving force for this

reaction is the available energy, or free energy, in the system. Figure 3.2 graphically shows a spontaneous free energy profile for the generic reaction, equation 1, providing the initial kinetics are favorable. The transition state is achieved when the reactants combine and form an intermediate which then produces C and D with lower energy.

Although the thermodynamic tendency is to reduce energy, this reaction will only take place if the initial energy barrier G*, the free energy of activation, is overcome. Mixing oxygen and hydrogen gas is a good example of a reaction that needs external energy to go towards completion. Without supplying energy to the gaseous mixture, it will not progress at a large rate even though it is very thermodynamically favorable. By providing energy, such as a spark, the initial energy barrier can be overcome and the

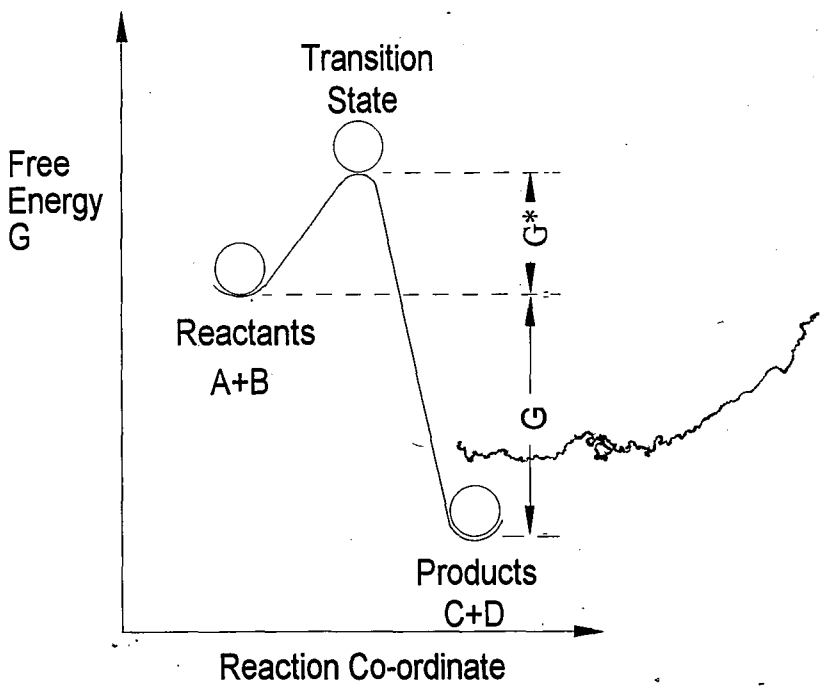

Figure 3.2: Free energy profile for the reaction which converts the reactants into products via a transition state. (Adapted from Trethewey et al.)

reaction can progress readily, an explosion in this case. This reaction can be reversed, but it requires an input of energy that is greater than or equal to G+G*. A finite amount of the products will be able to go backwards due to local high energies, but only on the molecular scale. In general, it is important to clarify that thermodynamics and kinetics are separate issues for corrosive processes and chemical reactions.

The energetics of these reactions is defined by the Nernst Equation,

$$E = E^{\circ} - \frac{RT}{zF}\log\frac{[\text{products}]}{[\text{reactants}]} \qquad \text{Eq. 2.}$$

E is defined as the electrochemical potential for the reaction, E° is the electrochemical potential at standard conditions (298 K and 1 atmosphere), z is the number of electrons transferred in the corrosion reaction, and the square brackets indicate the concentration values of the products and the reactants. R is the universal gas constant, T is the absolute temperature (K), and F is Faraday's constant. If the equilibrium values of concentrations at standard conditions are used, then E° can be determined since E is zero at equilibrium.[34]

Half cell reactions can aid in determining the direction of the reaction. If the energy for the half cell reaction of material A is e^{A} and e^{B} for material B, then the total energy for the reaction (E) is equal to the sum of the half cell reaction energies, or in equation form, $E = e^{A} + e^{B}$. The energies for many half cell reactions can be found in numerous places including the *Handbook of Chemistry and Physics*. A positive value for E leads to a negative value for G for the reaction, therefore the reaction will occur spontaneously from left to right. If E is negative and the kinetics are favorable, then the reaction process spontaneously from right to left. E establishes the preferred direction of the reaction, but not the rate (if it ever occurs at all).

The rate of reaction can be determined by measuring the current density of a material during corrosion. Using Faraday's Law, an expression for the corrosion rate, r, can be derived,

$$r = \frac{m}{tA} = \frac{ia}{nF} \qquad \text{Eq. 3}$$

where m is the amount of mass reacted, t is time, A is the surface area, *i* is the current density I/A in amps/cm^2, a is the atomic weight of the material, n is the number of electrons transferred, and F is Faraday's constant.[34] As the current density goes up, for a fixed potential, so does the rate of reaction. Furthermore, for a fixed current, as the surface area goes up the reaction rate slows down. By increasing the surface area of a protective coating, the corrosion resistance of the material can be prolonged.

3.4 CORROSION OF ALUMINUM IN PECVD APPLICATIONS

When a material is placed in an aqueous solution it can either be inert to that environment, corrode, or passivate. Often months or years are required to determine the outcome. Several factors that can affect a materials ability to remain inert are temperature, nature of the environment, and impurities in the alloy. Since most practical building materials are susceptible to corrosion (albeit in some cases at very slow rates) truly inert materials are very rare. Aluminum naturally self-passivates with atmospheric exposure, but this rarely yields enough protection in aggressive environments.

Passivation is defined as a very thin layer of a protective film which can, if damaged, quickly reform. Unfortunately in PECVD applications, natural passivation of the aluminum alloys does not provide enough protection; a more robust coating is needed

such as a hard anodization layer. Anodization layers are not deposited on the surface, they grow from the surface in, thus what is on the surface of the material prior to being anodized will also be present on the surface after anodization. This is one reason why alloying can affect the material's corrosive properties after anodization.

Focusing on the PECVD tool application, corrosion occurs in a more physio-chemical manner. Corrosion of the aluminum parts occurs due to the extremely aggressive environment. The most common mode of corrosion found for this application is blistering, which leads to scaling and particle generation. When a part reaches this level of corrosion it is said to have failed. The mechanism of failure is a complicated mixture of several different phenomena; 1) a surface reaction with fluorine, 2) diffusion of the fluorine through defects in the protective layer to the base metal, 3) another reaction between the fluorine and bare aluminum occurs to create aluminum fluoride (AlF_3), and 4) the growth of the AlF_3 blister to a size which causes the protective layer to scale and peel away.[36]

Chemical corrosion or dry oxidation of metals is defined as a chemical reaction involving only the chemical free energy, as opposed to the electrochemical free energy in aqueous solutions.[36] Generally this class of reactions occur at higher temperatures and the oxidation gas will form an interfacial layer by reaction with the surface of the metal as follows,

$$M + O_X \Leftrightarrow MO_X \qquad \text{Eq. 4,}$$

where O_X is the oxidizing species, (for PECVD cleaning applications, the halogenated compound), and M is the metal.

If this interfacial halogenated layer has low solubility in the plasma environment, then the reaction will slow or stop. If the solubility is high, then the reaction continues with the halogen diffusing further into the metal or the metal cations diffusing to the surface. The rate of this diffusion is inversely proportional to the interfacial layer thickness. The mass variation shows a parabolic dependence on time indicated in Eq. 5.

$$\Delta m = K_P t^{\frac{1}{2}} \qquad \text{Eq. 5.}$$

In this equation, Δm is the mass change due to corrosion, K_P is a constant, and t is time. As with most processes, raising the temperature increases the rate of the process following an Arrhenius law ,

$$\Delta m = A \exp(-\frac{\Delta E}{RT}) \qquad \text{Eq. 6,}$$

where ΔE is defined as the activation energy, R is the universal gas constant, and T is the absolute temperature.

To determine the rate limiting step of this process, we can look at the partial pressure of the oxidant halogen specie near the metal surface (P_{Ox}), the free energy of the reaction (ΔG^o) and the dissociation pressure of the reaction product (P_O) for the existing temperature (eq. 7).

$$\Delta G^O = -RT \ln(\frac{P_o}{P_{ox}}) \qquad \text{Eq. 7.}$$

If the P_{Ox} is greater than that of P_O, the protective halogenated layer will be stable and the metal will be oxidized. If the opposite is true, then the protective layer will be

unstable and the metal can be considered to be more noble than the oxidation reaction and will not be oxidized, thus showing immunity to the environment.

From the above discussion, several desirable properties for a protective layer can be identified in engineering long lasting parts for PECVD applications. Higher surface area in contact with the aggressive environment will reduce the corrosion rate for a fixed amounts of reactants. Choosing appropriate alloying agents can inhibit halogen diffusion, and minimizing the time the parts are wetted by the aggressive environment or even choosing a less aggressive environment can markedly improve corrosion resistance. Only recently, have these three suggestions been investigated for implemention into today's production tools.[33,37]

An additional of concern in PECVD systems, that differs from the typical corrosive environments, is ion bombardment of the surface in capacitively coupled rf plasma systems. Ions are accelerated across the sheath and impact the surface of the aluminum parts adding additional energy for surface reactions to occur or even possibly sputtering the oxide layer away. Also, the PECVD deposition steps are typically performed at elevated temperatures, ~ 450 C. The high temperatures, while not unique to this application, do compound the issue by supplying additional energy to the aluminum parts for activation of corrosion mechanisms. The excess energy (plasma and thermal) causes premature degradation of the aluminum parts. This work strives to examine ways to enhance the corrosion resistance and increase the lifetime of the parts.

4.0 RESULTS AND DISCUSSION

4.1 CHARACTERIZATION OF THE "AS RECEIVED" SAMPLES

The composition of the different alloys investigated is listed in table 1. The major differences between them are the levels of magnesium, chromium, silicon and iron. There are several other important differences between these alloys that should be noted. Alloy 6061 is a precipitation hardened material. This is done to add strength to the alloy. However, the alloy 5352 is a solid solution strengthened alloy with higher magnesium concentration.

Alloy	Si (wt. %)	Fe (wt. %)	Mg (wt. %)	Mn (wt. %)	Cr (wt. %)	Al (wt. %)
6061 T6	0.40-0.80	0.7 max.	0.8-1.2	0.15	0.04-0.35	rem.
5352	0.05	0.06	2.2-2.8	0.09	0.10 max.	rem.

Table 1 : Composition of aluminum alloys 6061 and 5352.[38]

Visually there is a distinct difference in the anodized alloys. Figure 4.1 is a photograph of the different alloys in their "as received" condition. The alloy 5352 anodized samples maintain a silver sheen in comparison to alloy 6061. Darkening of the anodized alloy 6061 is due to the alloying agents and precipitates found in 6061 T6, particularly iron, silicon, and manganese. These alloying agents form intermetallic compounds with the aluminum which are in turn incorporated into the anodization layer which can lead to defects in the oxide layer. The combination of oxide defects and impurity inclusions, result in the characteristic dark appearance of anodized 6061 T6 alloy.

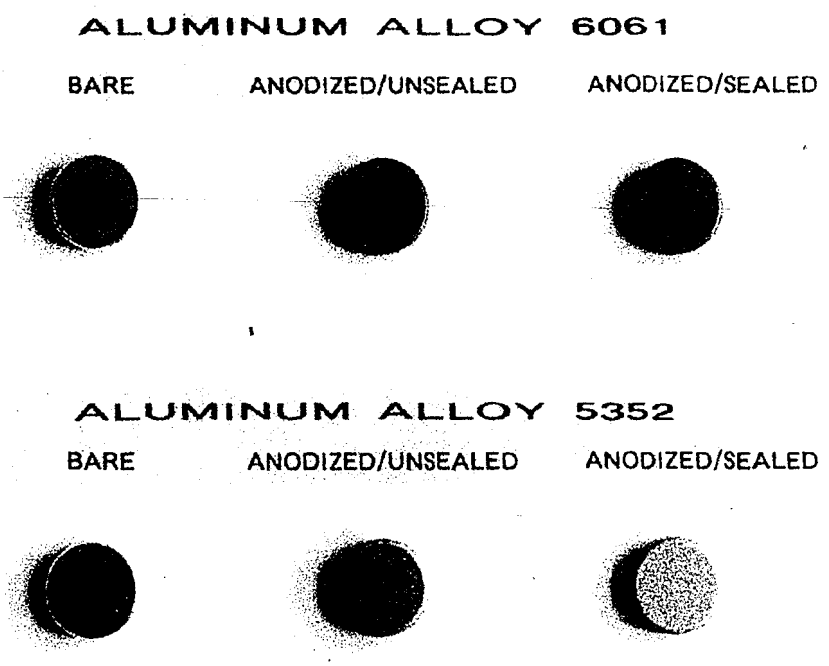

Figure 4.1: Photograph of the six different sample types. Visually the 5352 anodized samples have a much different appearance than the 6061 counterparts.

The alloy 5352 samples have higher magnesium content and lower silicon and iron levels compared to the alloy 6061 samples. Alloy 5352 has minimal precipitates present that can lead to anodizing layer defects, while ,by design, alloy 6061 has mainly Mg_2Si precipitates to aid in strengthening of the alloy. The low levels of iron and silicon and solid solution of magnesium lead to a high purity, dense aluminum oxide formed by anodizing. This is the reason for the translucent or silver sheen appearance.

The last major factor leading to a difference in appearance is that the alloy 5352 samples were in the "as cast" condition while the 6061 samples were taken from rolled plate. The "as cast" material results in rough appearance due to the larger grain sizes, while the plate is more uniform in surface texture and smaller grain size by design.

4.2 GENERAL XPS ANALYTICAL PROCEDURE

Software supplied by Physical Electronics Corporation, PC Explorer for DPCMA version 3.4, is used to collect the XPS depth profile spectra. The software controls the acquisition of the XPS data and sputter intervals. A cycle of the depth profile is defined as a multiplex acquisition and a sputter interval. For most of these experiments, the depth profiles consisted of 14 cycles. The first two cycles of each depth profile had no sputter cycle. This was done to evaluate the surface concentrations twice before sputtering and is built into the software. The sputter intervals were set to be 5 minutes, or a total sputter time of 60 minutes for each sample.

Multiplex spectra were acquired, the individual regions were curve fit to determine the peak areas and peak positions, since this information yields the chemical bonding information and makes XPS a valuable technique for surface analysis. Physical Electronics Corporation curve fitting software, Multipak version 2.0 , was used to perform this task. It uses MATLAB, a registered trademark of The Mathworks, Inc., version 4.00.950 as the math engine to perform the necessary calculations needed for curve fitting.

The acquired spectra were loaded into Multipak and were curve fit using the following method. No smoothing of the data was performed as the intensity of most peaks was sufficient to get reproducible fit parameters. The data were Shirley background corrected and the baseline set to maximize the peak area for all elemental peaks. Except for a few cases (anodized and sealed "as received" samples) all data were collected as a depth profile. By collecting the data in this manner, all scans for the entire profile for one element were viewed at once. This allowed the baseline to be fixed for all the individual

fits for each element in that profile. The fits were constrained to a full width at half maximum of 2.5 max., and no less than 70 % Gaussian curvature. The other samples were depth profiled manually, duplicating the automatic sequence. The high resolution spectra were then curve fit and the results were compiled, analyzer sensitivity corrected, and tabulated to produce depth profile graphs for each sample.

Spectra seen in figure 4.2-4.5 were taken after the first sputter period in each depth profile. This allowed comparison of the peak intensities and areas after removal of spurious contamination. Depth profile plots were generated by curve fitting each element in each cycle and using the integrated peak areas. The peak areas were then divided by the appropriate atomic sensitivity factor for the analyzer, provided by Physical Electronics.[13] Summing all the corrected peak areas gave the total area for the cycle, sum_C. The total elemental corrected peak area was then divided by sum_C resulting in the atomic percentage of that element. Graphs were generated plotting atomic concentrations as a function of depth into the sample surface, which are discussed in section 4.3 and 4.4.

The sputter depth was calculated by multiplying the duration of the sputter interval, typically 5 minutes, by the sputter rate determined from the sputter calibration curve in figure 2.3, 8.3 angstroms (Å) per minute. The result was the depth, in angstroms, into the surface or the sputter depth. Also, each depth profile had two multiplexes completed before the initial sputter period. Both pre-sputter multiplex concentrations are depicted on the plot; the first concentration level is plotted as a negative surface depth and the second concentration is plotted at the zero depth position, for visual purposes only.

Aluminum oxide is an insulating material and therefore will charge upon exposure to ionizing radiation. This charging will shift the observed binding energy of the photoelectrons to higher energies. The most common way of correcting for this is to reference the C (1s) peak of adventitious carbon peak to be 285.0 eV. Since these samples contained very little adventitious carbon, a different charge correction scheme was used. The oxygen (1s) peak was used to correct for sample charging.[39] For the "as received" samples, the oxygen (1s) peaks were reduced in binding energy to the accepted value of the aluminum-oxygen binding energy, 531.6 eV, of aluminum oxide Al_2O_3. The other peak positions were then reduced in energy by the same amount. The accepted binding energy for aluminum metal (2p) peak is 74 eV, aluminum oxide (2p) is 74.7 eV, magnesium (1s) is 1304 eV, and fluorine (1s) is 684.9 eV.[13]

By performing the appropriate correction for each spectrum, the chemical information could be extracted. "As received" XPS spectra for the aluminum and oxygen regions for each alloy are presented in figures 4.2 and 4.3, respectively for alloy 6061 and 5352. For all the presented curve fits in figures 4.2-4.5, the corrected binding energy and peak areas are stated in table 2. The "as received" analysis for each alloy were quite similar. The aluminum spectra showed a single peak which was attributed to Al_2O_3. Oxygen had a two component peak whose main component was also attributed to Al-O bonding and a minor higher energy component, due to about 5% of oxy-fluoride formation. The fluorine in these spectra was due to minor fluorine contamination of the sample load lock.

Figures 4.4 and 4.5 display the aluminum, oxygen, fluorine and magnesium regions

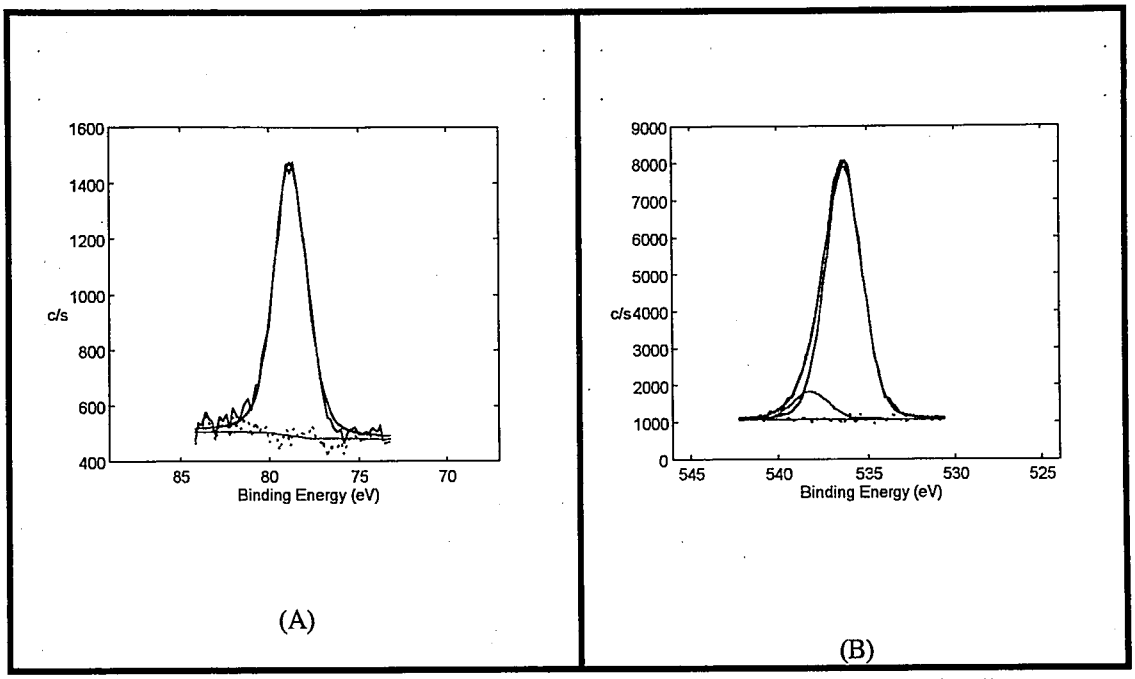

Figure 4.2: XPS aluminum (A) and oxygen (B) spectra for an "as received" alloy 6061 anodized/unsealed sample.

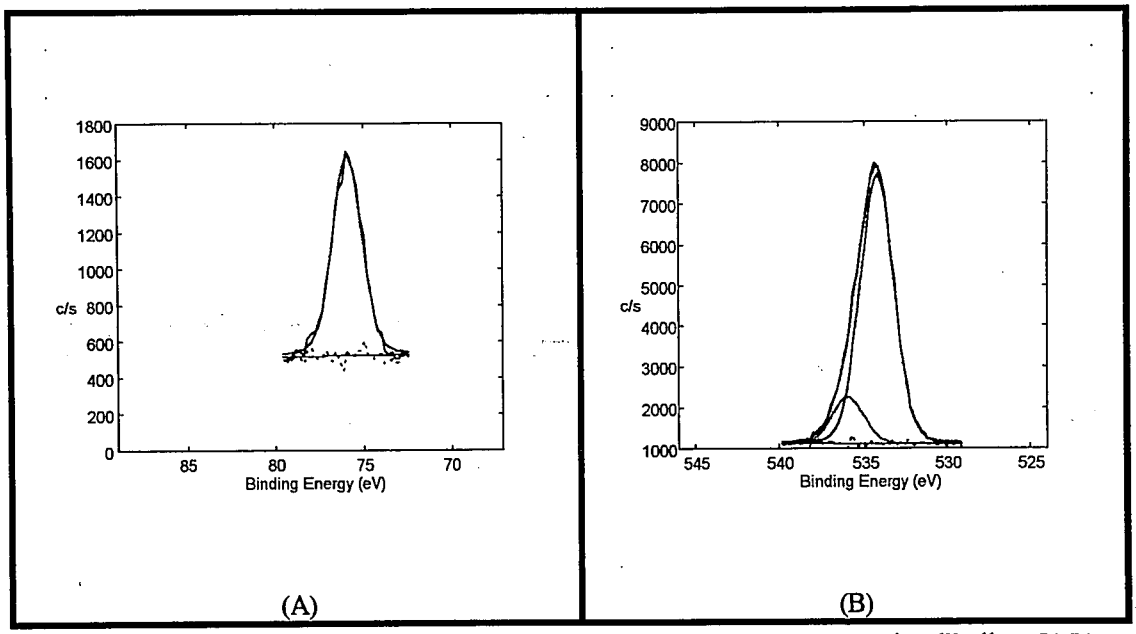

Figure 4.3: XPS aluminum (A) and oxygen (B) spectra for an "as received" alloy 5352 anodized/unsealed sample.

for the room temperature exposed samples for anodized and unsealed alloy 6061 and 5352, respectively. The aluminum spectra reveals an additional component at 2.4 eV higher in binding energy which can be assigned to the formation of aluminum oxy-fluoride, AlO_XF_Y. Intensities of the oxy-fluoride components of the Al and O spectra were greater for alloy 6061 than for alloy 5352, indicating poorer corrosion resistance characteristics for alloy 6061. Magnesium, which was not observed in the "as received" spectra, was present for both alloys post-exposure, but was more intense for alloy 5352.

			Alloy 6061		Alloy 5352	
			Low	High	Low	High
As Received Samples	Energy (eV)	Al (2p)	74.1		73.4	
	Area (arb)		23482		22964	
	Energy (eV)	O (1s)	531.6	533.5	531.6	533.3
	Area (arb)		29651	3119	27289	4481
Post NF_3/Ar Plasma Exposure Samples	Energy (eV)	Al (2p)	72.9	75.2	73.6	76.0
	Area (arb)		8227	2218	9955	282
	Energy (eV)	O (1s)	531.6	532.9	531.6	533.3
	Area (arb)		8705	2690	14914	1311
	Energy (eV)	F (1s)	685.6	686.8	686.1	687.3
	Area (arb)		10970	4112	7735	1011
	Energy (eV)	Mg (1s)	1307.1		1306.8	
	Area (arb)		306		920	

Table 2: Representative corrected binding energies (eV) and peak areas (arbitrary units) for "as received" and plasma exposed samples.

The XPS depth profiling analysis was completed using two x-ray anodes. The anodized and unsealed samples were completed using an aluminum anode and the others were completed using a magnesium anode. The use of the aluminum anode, which has a higher energy K_α x-ray than the magnesium K_α x-ray, allowed the Mg 1s region to be monitored. This region has a higher atomic sensitivity factor than the Mg 2p region.

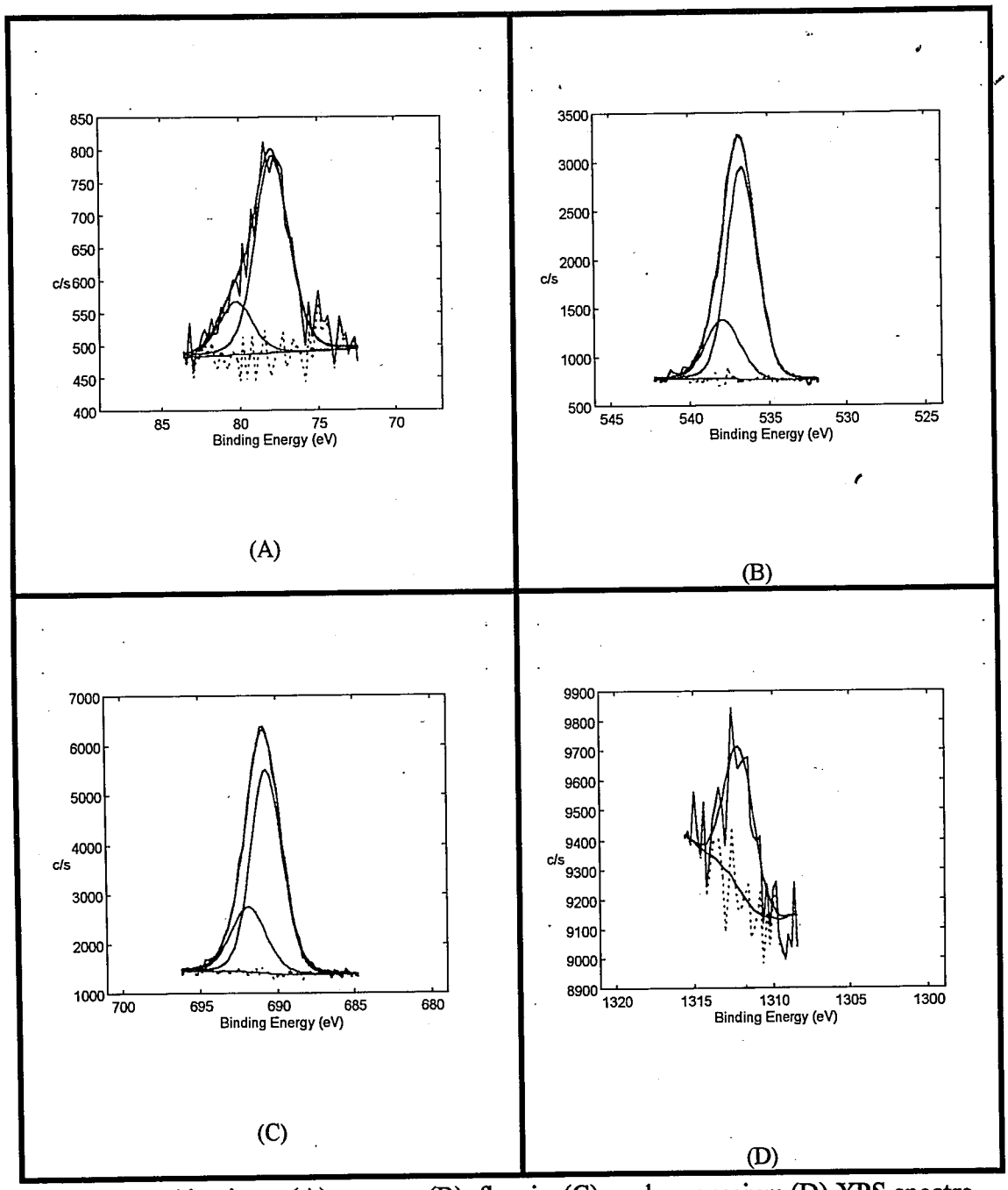

Figure 4.4: Aluminum (A), oxygen (B), fluorine(C) and magnesium (D) XPS spectra for a room temperature NF_3/Ar plasma exposed alloy 6061 anodized/unsealed sample.

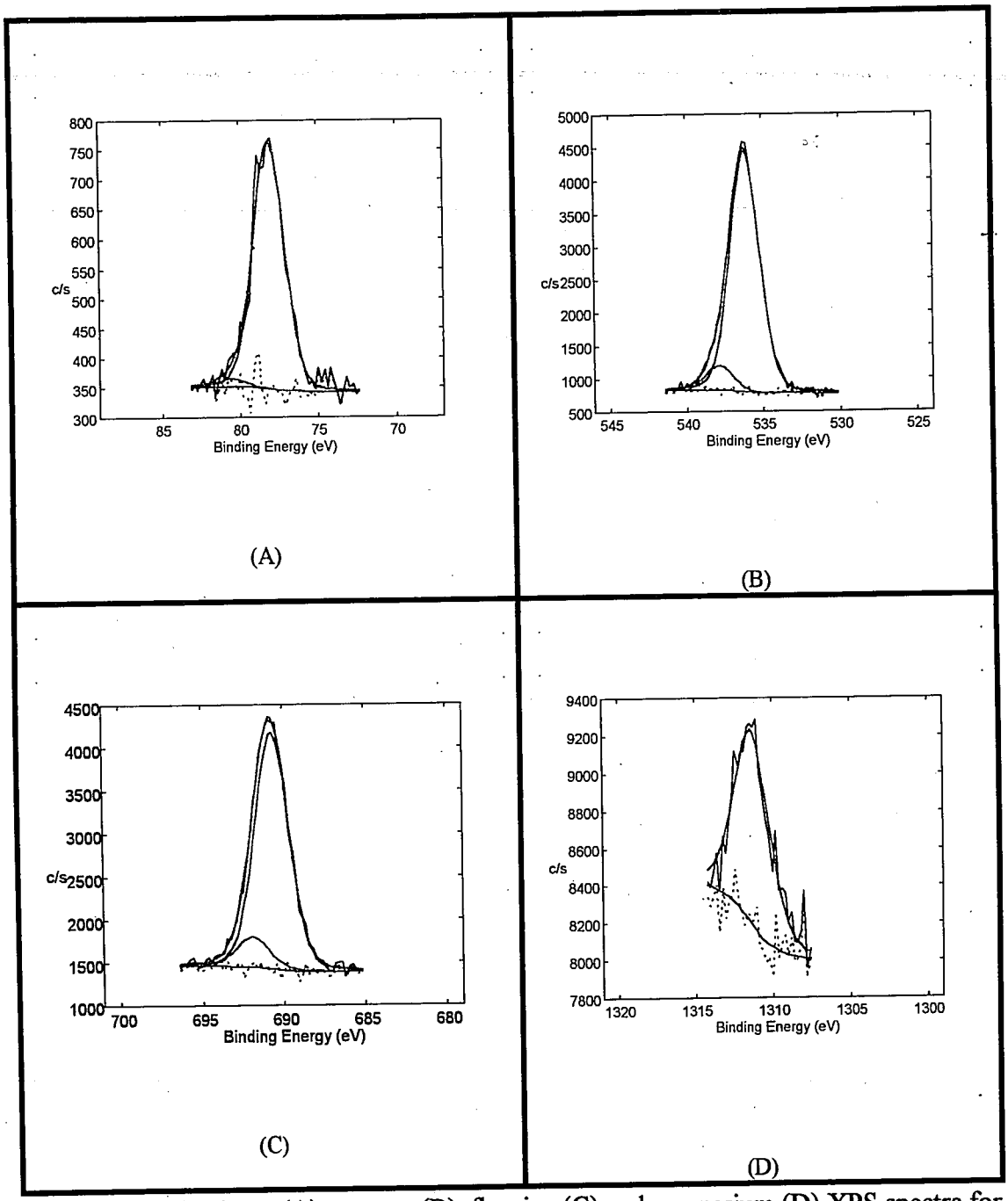

Figure 4.5: Aluminum (A), oxygen (B), fluorine (C) and magnesium (D) XPS spectra for a room temperature NF_3/Ar plasma exposed alloy 5352 anodized/unsealed sample.

4.3 "AS RECEIVED" SAMPLE DATA ANALYSIS

Cross sectional SEM images of the "as received" anodized/unsealed alloy 6061 (figure 4.6) and alloy 5352 (figure 4.7) samples are shown with the superimposed ZAF corrected atomic concentrations plotted versus distance across the anodization layer. Alloy 6061 anodized/unsealed samples had the expected stoichiometric aluminum oxide layer with about 3% sulfur, (from the anodization chemistry), incorporated in the anodized layer which was not incorporated into the bulk aluminum. The interface was very sharp between the oxide layer and the base metal. Alloy 5352 anodized/unsealed samples had the same amount of sulfur incorporated into the anodization layer; the magnesium and silicon levels in the coating were consistent with the alloy concentration.

"As received" XPS depth profiles for the alloy 6061 samples (bare, anodized/ unsealed, and anodized/sealed) are shown in figures 4.8, 4.9, and 4.10. The fluorine present in all "as received" profiles was a result of minor fluorine contamination to the load lock system. In all cases, the fluorine levels were less than 2.0% in the bulk material and less than 5.0% on the surface. These depth profiles determined the baseline oxygen and aluminum levels for each alloy. Alloy 6061 anodized samples had a bulk composition of approximately 55% and 35% for oxygen and aluminum, respectively. The bare sample had 90 % aluminum: the remaining 10% consisted of the major alloying agents, silicon and magnesium, and adventitious carbon from atmospheric exposure prior to analysis. Sulfur was also present in the anodization layer (as evidenced by the EDS analysis), but was below the limit of detection for the XPS instrument. There was no difference in baseline concentration between the unsealed and sealed samples for either alloy.

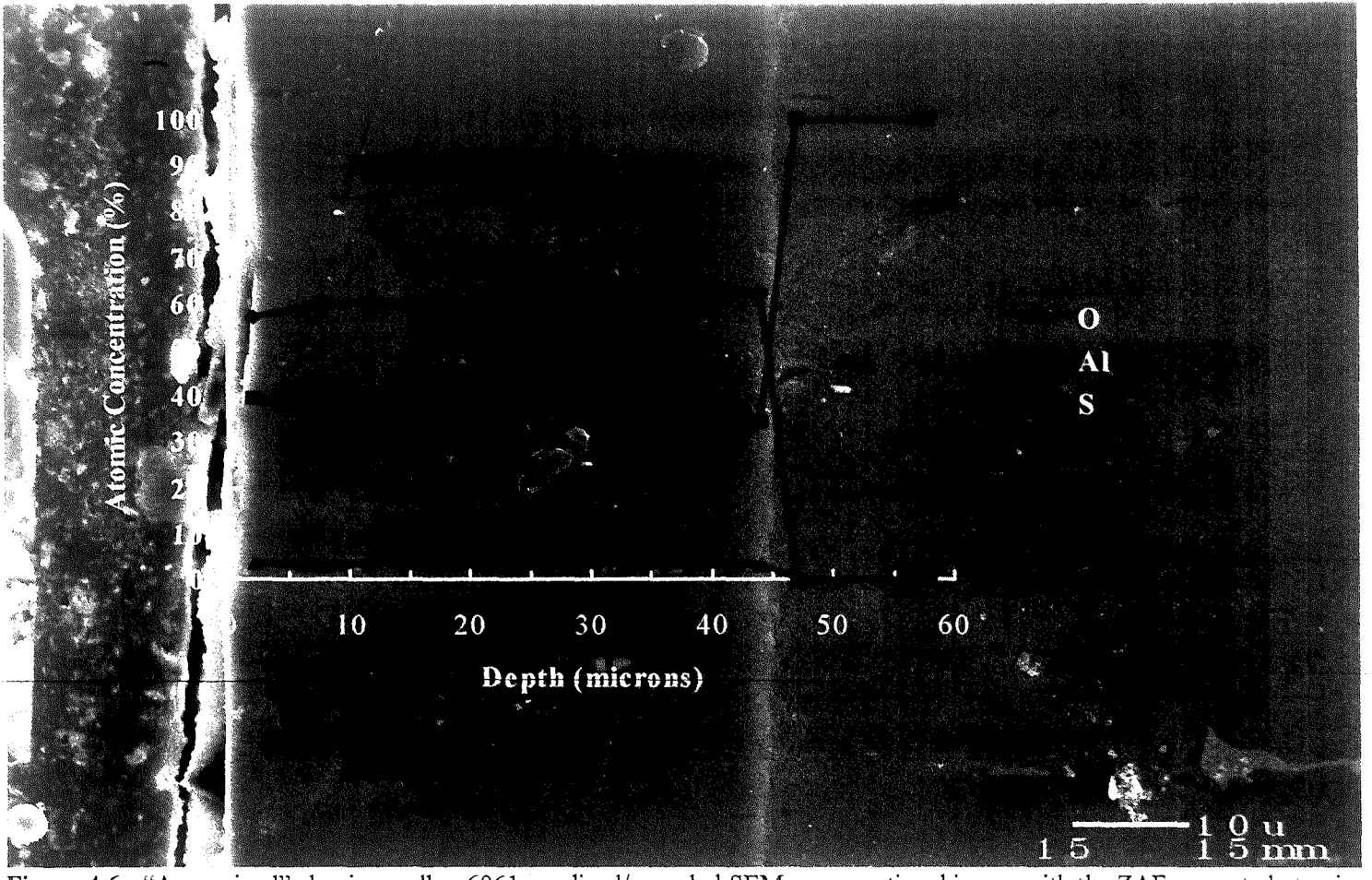

Figure 4.6: "As received" aluminum alloy 6061 anodized/unsealed SEM cross sectional image with the ZAF corrected atomic concentrations plotted versus depth across the anodization layer. This shows a stoichiometric anodization layer with about 3 % sulfur incorporated due to the anodization chemistry.

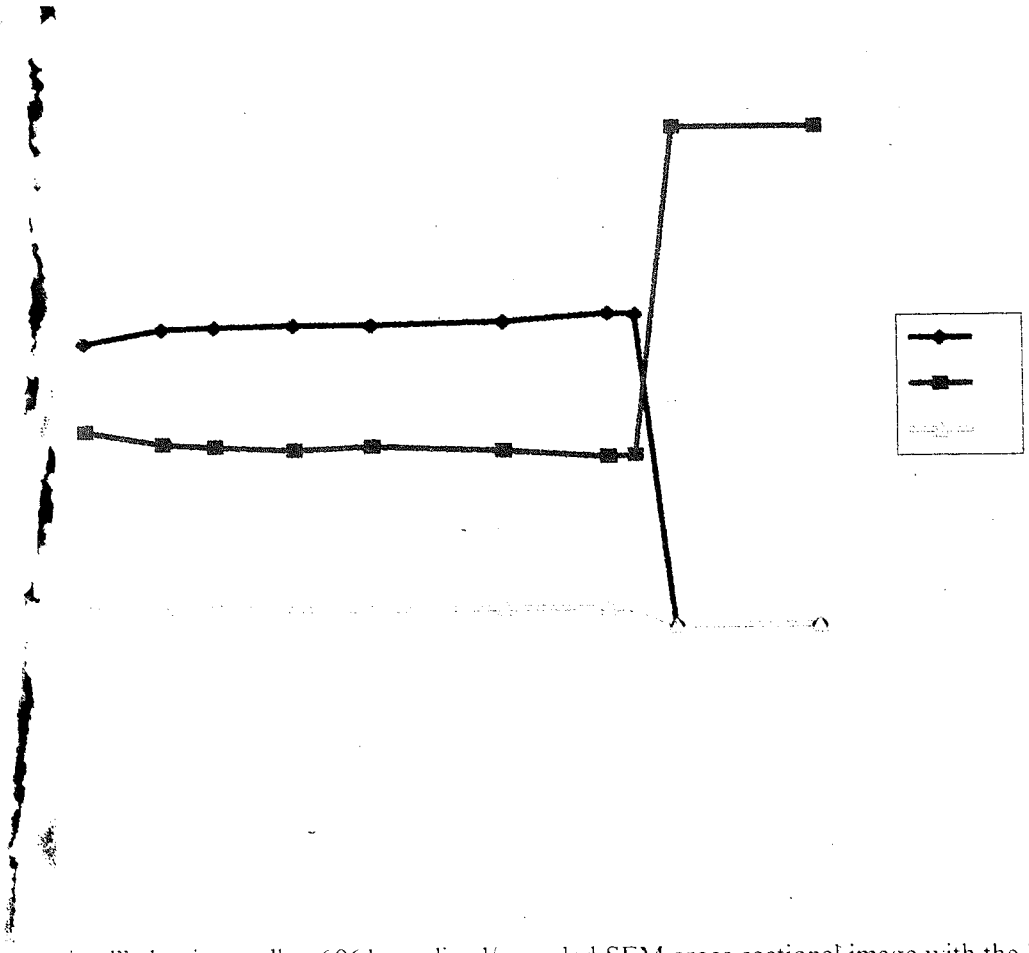

Figure 4.6: "As received" aluminum alloy 6061 anodized/unsealed SEM cross sectional image with the ZAF corrected atomic concentrations plotted versus depth across the anodization layer. This shows a stoichiometric anodization layer with about 3 % sulfur incorporated due to the anodization chemistry.

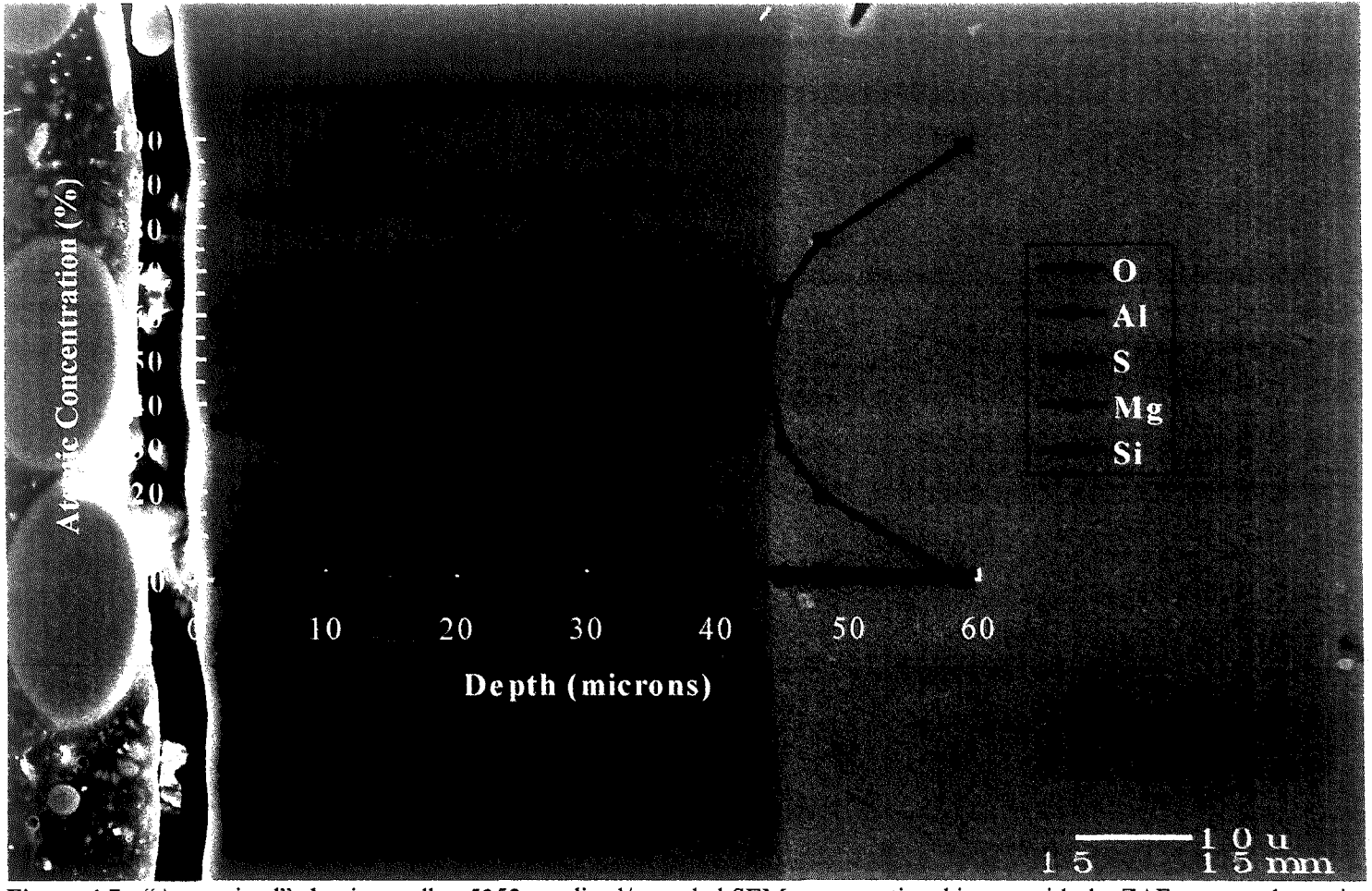

Figure 4.7: "As received" aluminum alloy 5352 anodized/unsealed SEM cross sectional image with the ZAF corrected atomic concentrations plotted versus depth across the anodization layer. This shows a stoichiometric anodization layer with about 3 % sulfur and traces of magnesium and silicon.

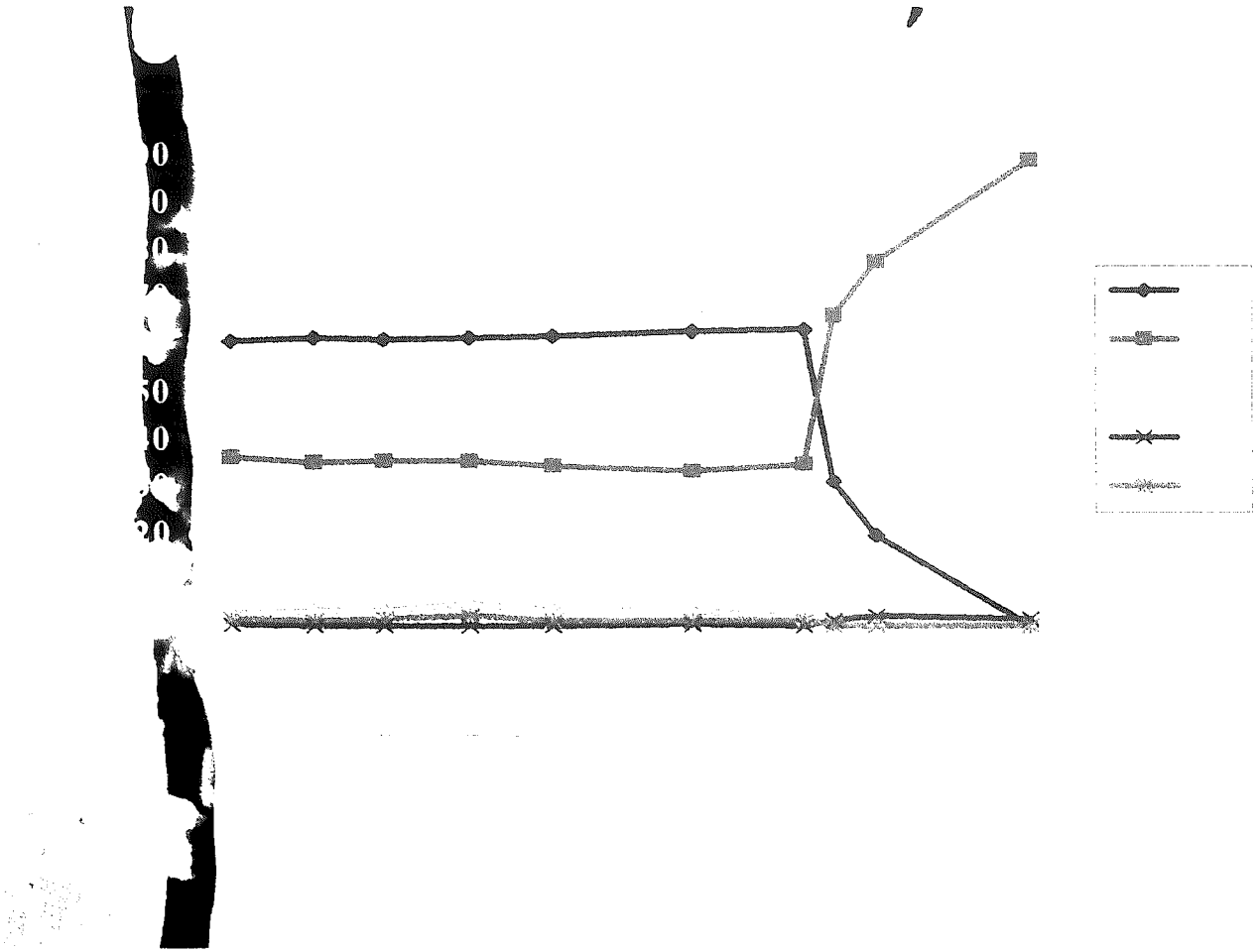

Figure 4.7: "As received" aluminum alloy 5352 anodized unsealed SEM cross sectional image with the ZAF corrected atomic concentrations plotted versus depth across the anodization layer. This shows a stoichiometric anodization layer with about 3 % sulfur and traces of magnesium and silicon

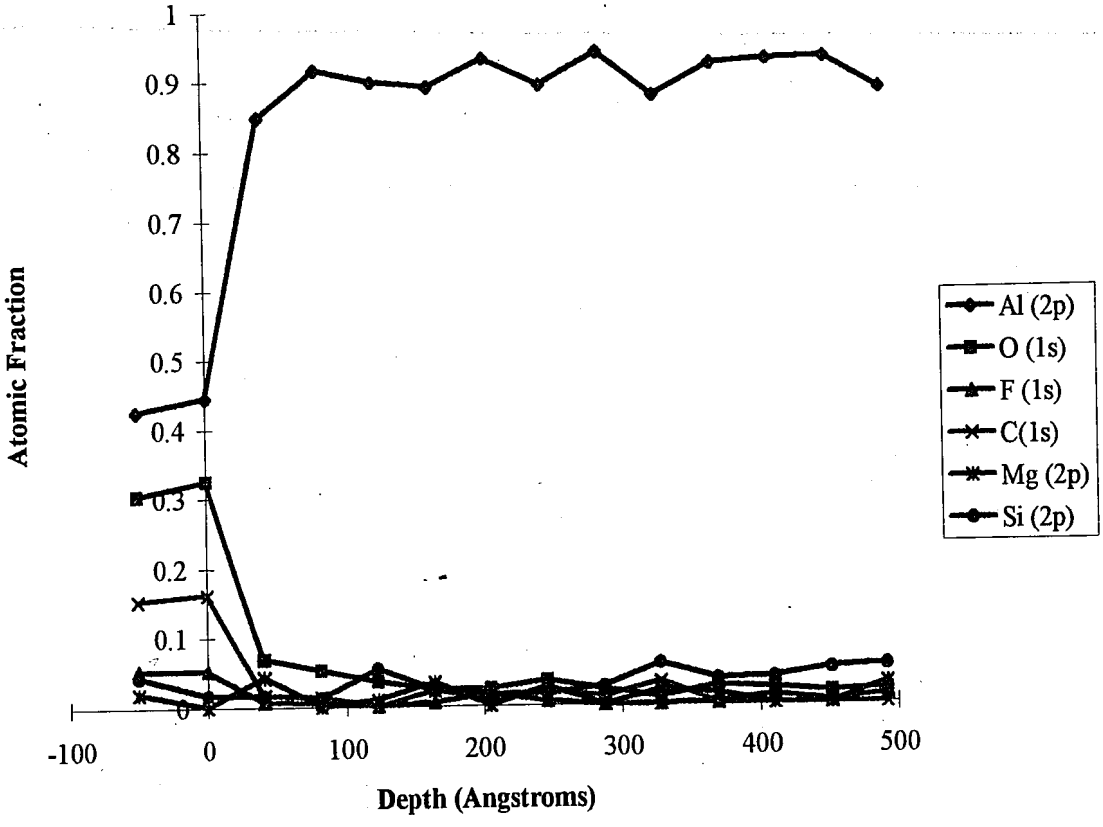

Figure 4.8: XPS depth profile of "as received" bare aluminum alloy 6061 sample.

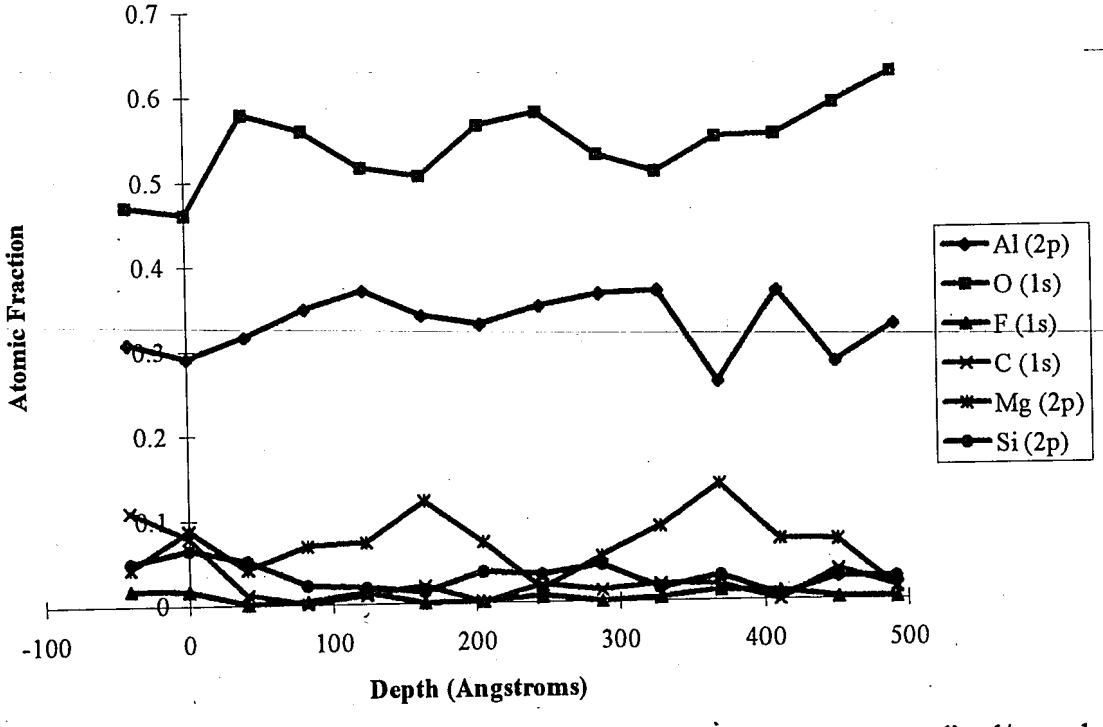

Figure 4.9: XPS depth profile of an "as received" aluminum alloy 6061 anodized/unsealed sample.

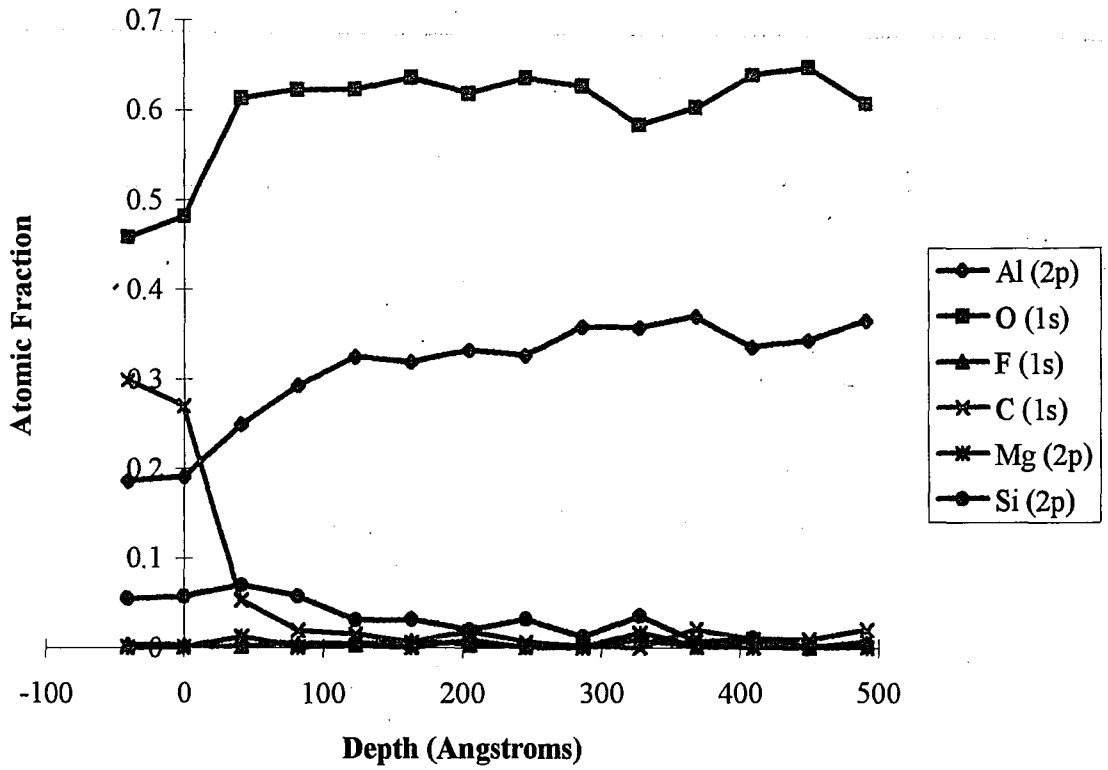

Figure 4.10: XPS depth profile of an "as received" aluminum alloy 6061 anodized/sealed sample.

"As received" XPS depth profile analysis for the alloy 5352 bare sample (figure 4.11) revealed a thin layer of surface oxide and carbon. Aluminum metal made up 90 % of the bulk material with the remainder consisting of magnesium and silicon. The bulk oxygen and aluminum atomic concentrations for the anodized/unsealed sample (figure 4.12) and the anodized/sealed sample (figure 4.13) were both about 50% and 45 %, respectively. The remainder, about 5 %, was made up of magnesium and silicon. Alloying agents were homogeneously dispersed throughout the samples.

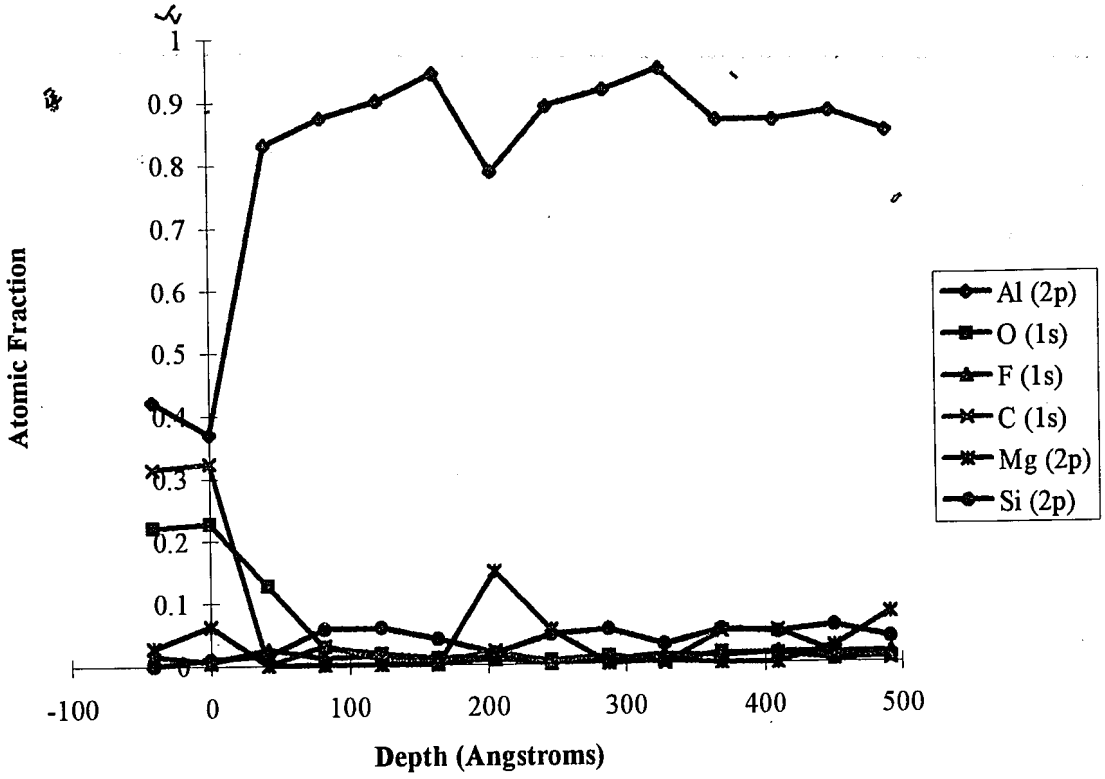

Figure 4.11: XPS depth profile of "as received" bare aluminum alloy 5352 sample.

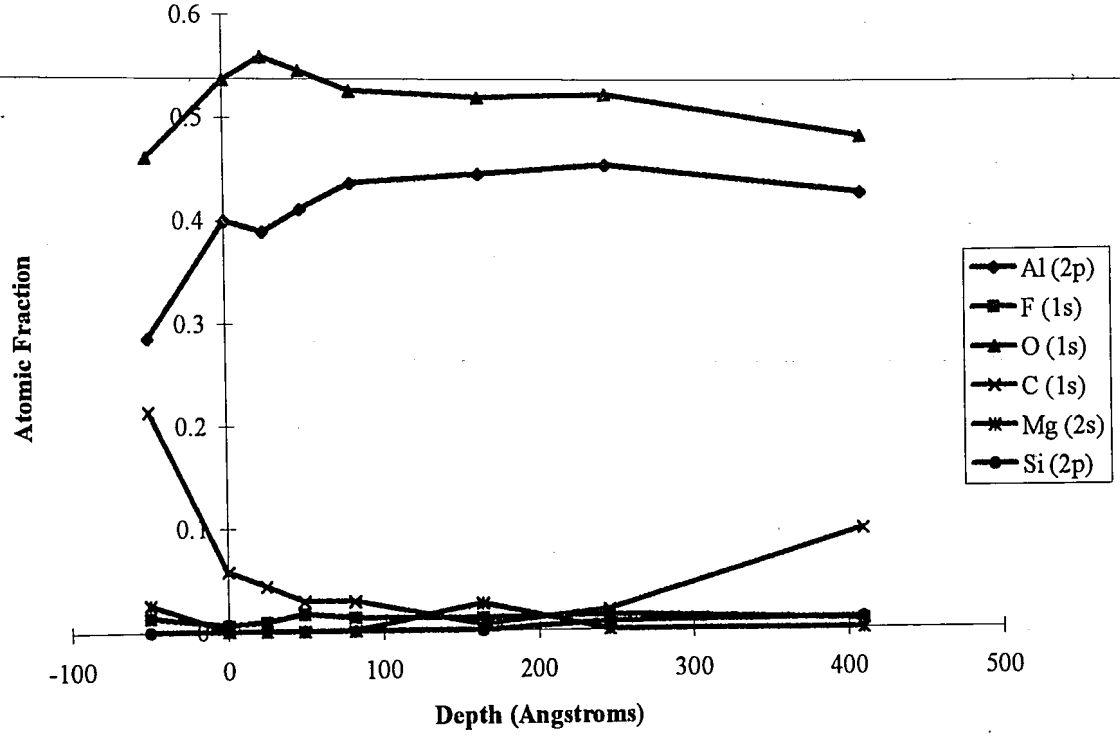

Figure 4.12: XPS depth profile of "as received" aluminum alloy 5352 anodized/unsealed sample.

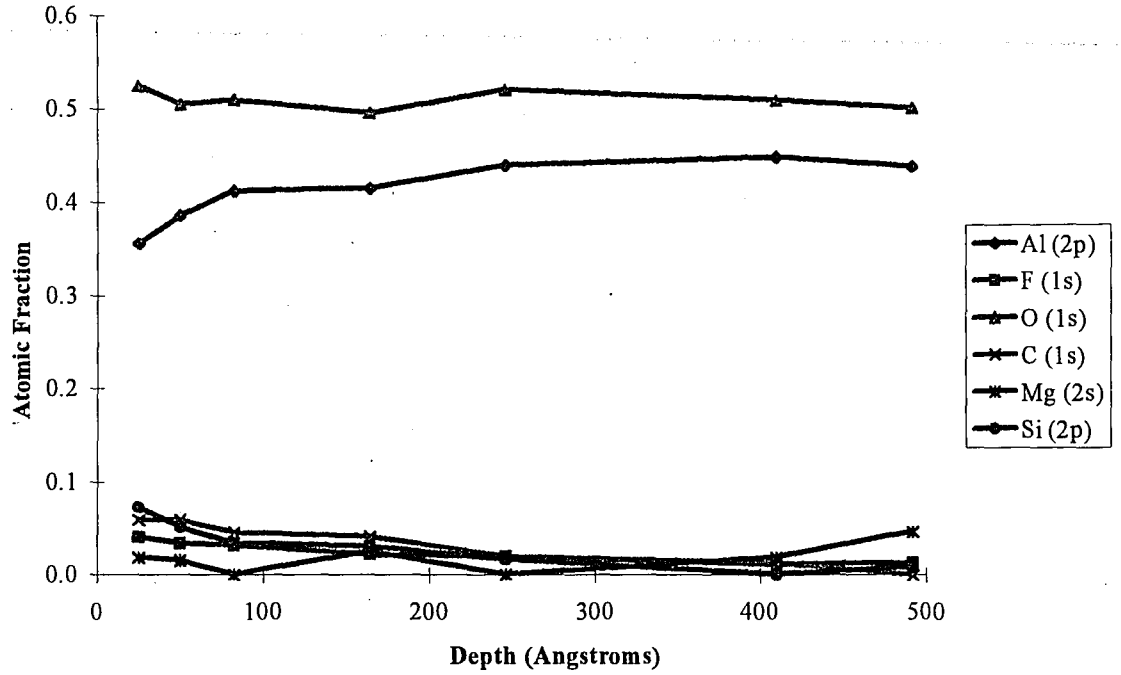

Figure 4.13: XPS depth profile of an "as received" aluminum alloy 5352 anodized/sealed sample.

4.4 PLASMA EXPOSED SAMPLE DATA ANALYSIS

The superimposed atomic concentration plots for the plasma exposed SEM and EDS analysis should only be used as trend lines due to the uncertainty associated with the unpolished surface. Also, these samples were vented to the atmosphere and cut using a diamond saw prior to SEM and EDS analysis. Alloy 6061 anodized/unsealed plasma exposed at 450 C sample (figure 4.14) had fluorine present 40 μm into the anodized layer. The magnesium showed a spike approximately 10 μm from the surface, everywhere else it was not detected.

EDS analysis of the alloy 5352 anodized/unsealed plasma exposed at 450 C sample (figure 4.15) showed the fluorine concentration dropped more rapidly but was still

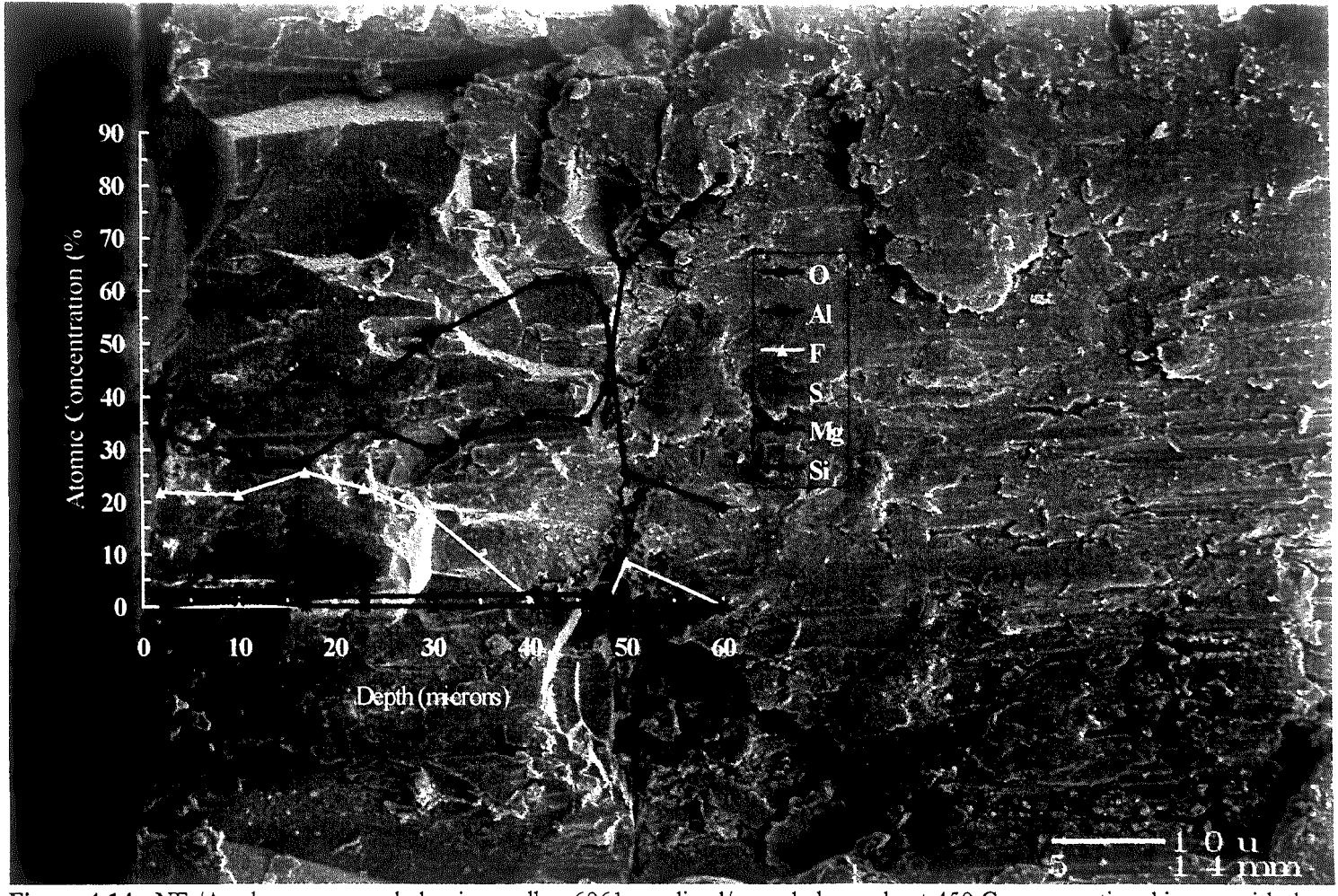

Figure 4.14: NF_3/Ar plasma exposed aluminum alloy 6061 anodized/unsealed sample at 450 C cross sectional image with the ZAF corrected atomic concentrations plotted versus depth across the anodization layer.

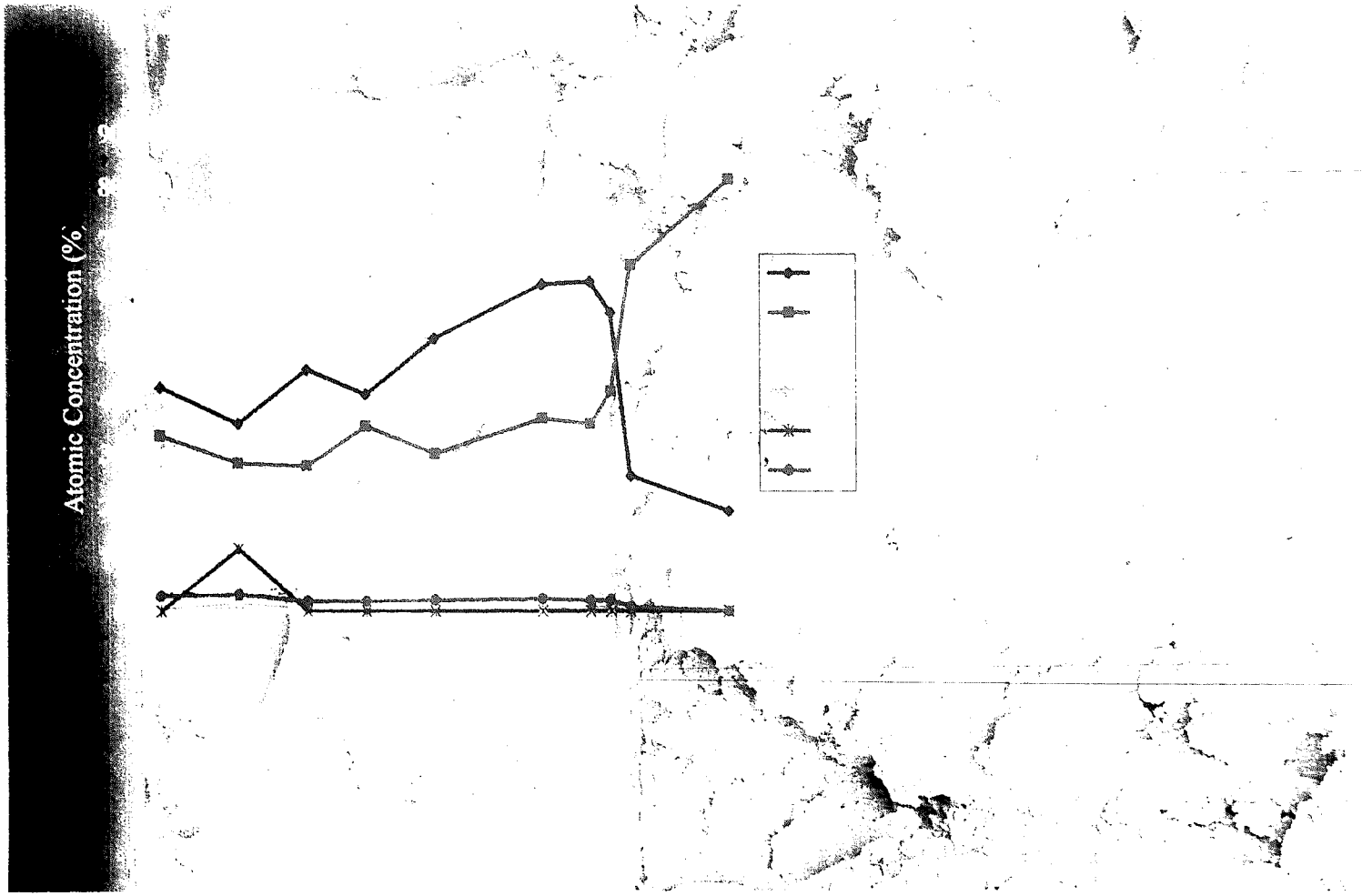

Figure 4.14: NF_3/Ar plasma exposed aluminum alloy 6061 anodized/unsealed sample at 450 C cross sectional image with the ZAF corrected atomic concentrations plotted versus depth across the anodization layer.

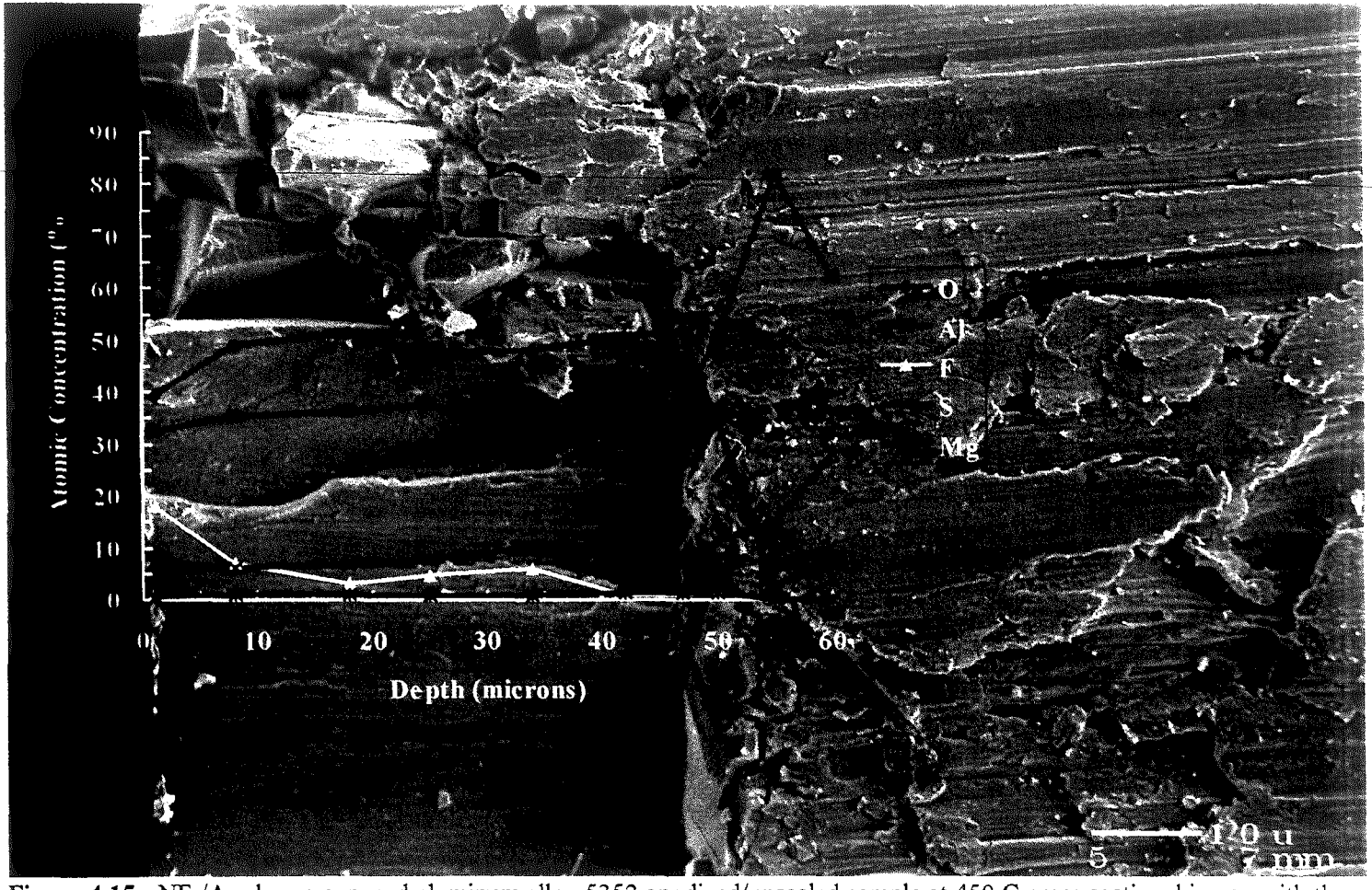

Figure 4.15: NF_3/Ar plasma exposed aluminum alloy 5352 anodized/unsealed sample at 450 C cross sectional image with the ZAF corrected atomic concentrations plotted versus depth across the anodization layer. The rise in sulfur past the interface is an artifact created by the saw blade.

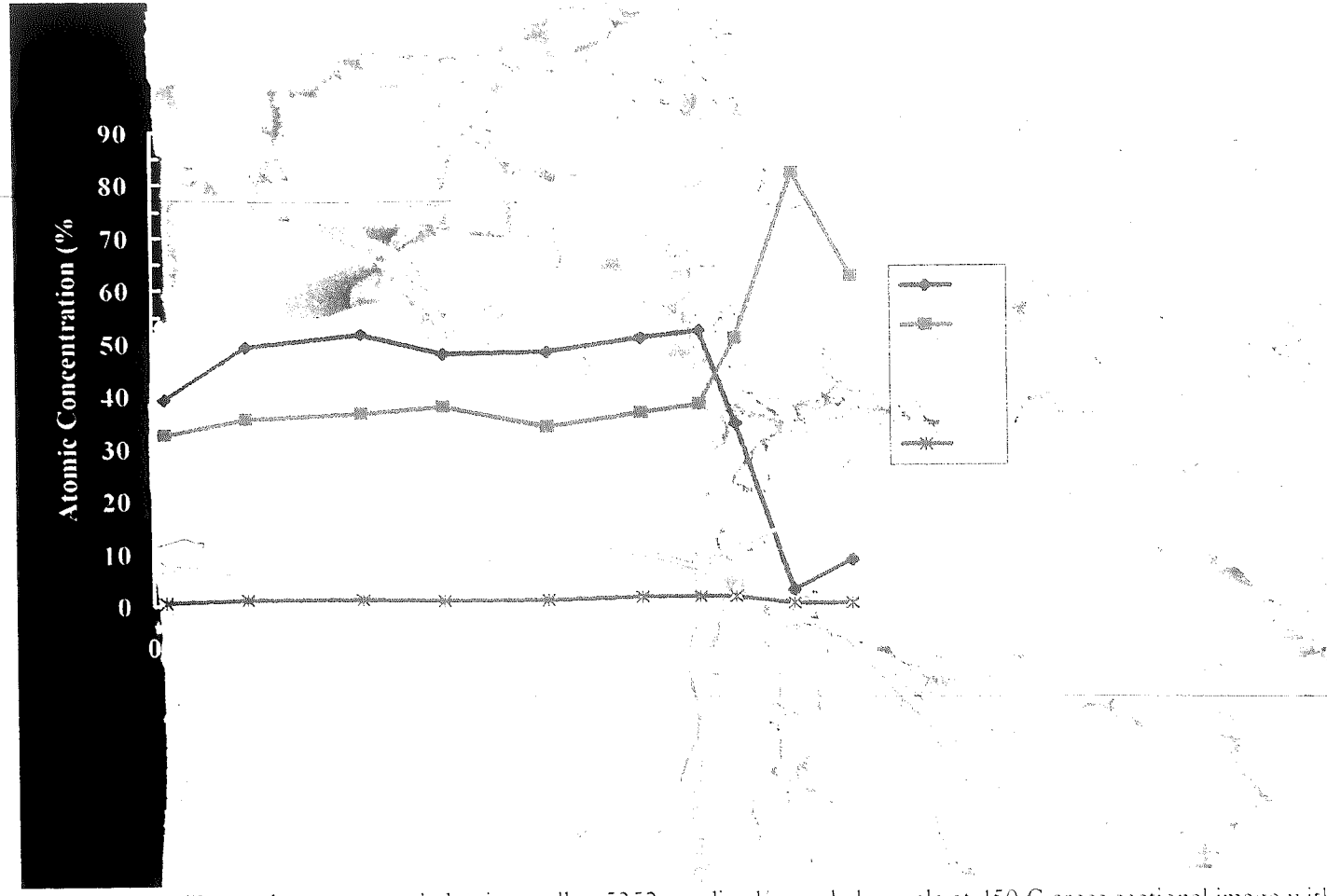

Figure 4.15: NF_3/Ar plasma exposed aluminum alloy 5352 anodized/unsealed sample at 450 C cross sectional image with the ZAF corrected atomic concentrations plotted versus depth across the anodization layer. The rise in sulfur past the interface is an artifact created by the saw blade.

present, in low levels, deep into the anodization layer. The decrease in fluorine concentration corresponded to an increase in magnesium concentration, followed by a depleted magnesium region. This suggests that magnesium plays a role in the higher fluorine corrosion resistance of anodized/unsealed alloy 5352 sample.

XPS analysis of the bare aluminum 6061 sample, upon room temperature NF_3/Ar plasma exposure (figure 4.16), showed extensive fluorine incorporation into the surface, nearly 300 Å. The resulting surface layer consisted of aluminum fluoride. An arbitrary benchmark of 10% atomic fluorine concentration was used for comparing corrosion resistance. The fluorine concentration for the plasma exposed bare 6061 sample did not dip below 10% until approximately 400 Å into the sample surface. At this point, the magnesium concentration began to increase.

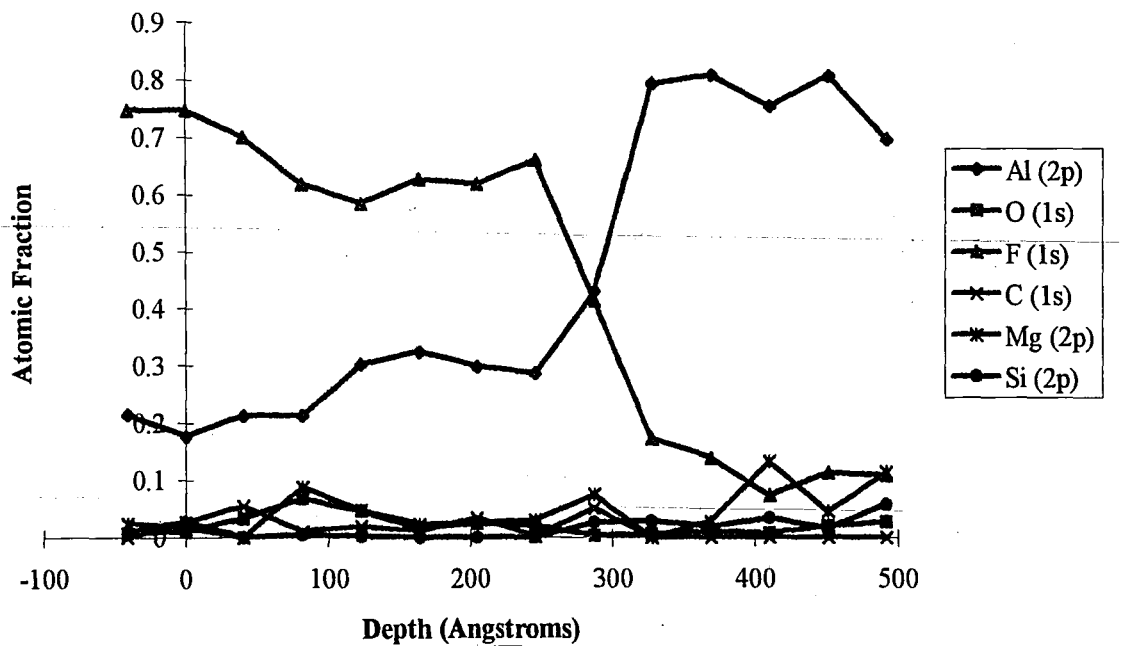

Figure 4.16: XPS depth profile of an NF_3/Ar plasma exposed at room temperature bare aluminum alloy 6061 sample.

Analysis of the plasma exposed bare alloy 5352 sample (figure 4.17) showed very high levels of fluorine incorporation at the surface. The fluorine concentration did not drop below 10 % until after about 550 Å. Magnesium concentration increases coincided with fluorine concentration decreases. The alloy 5352 bare sample had less resistance to fluorine incorporation than the 6061 bare alloy.

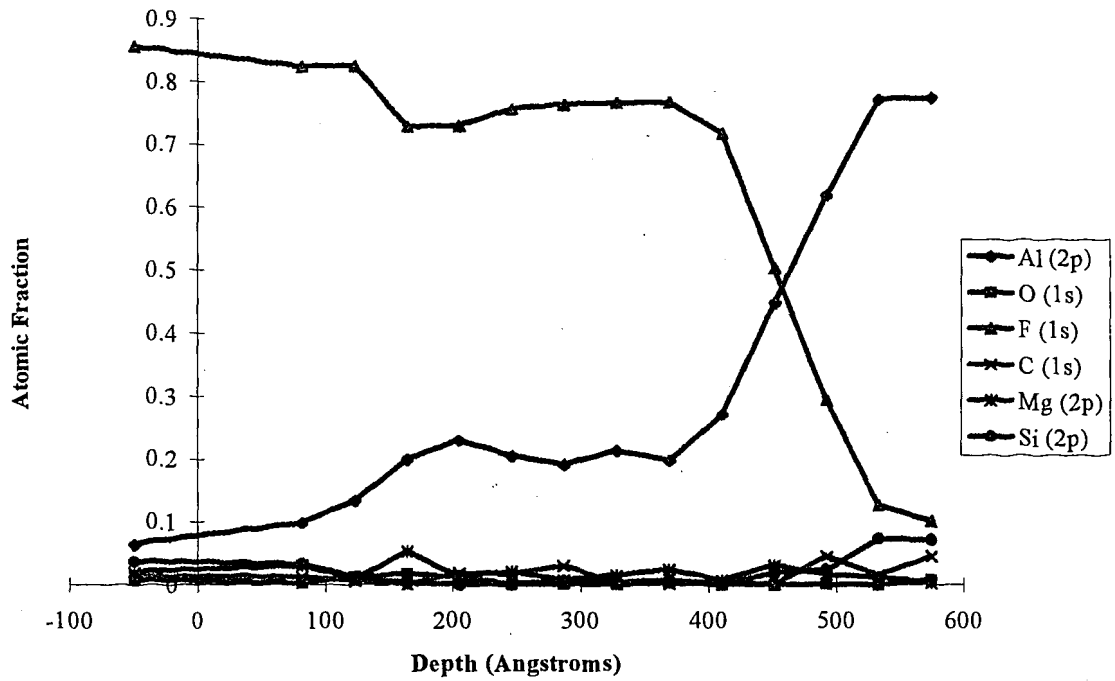

Figure 4.17: XPS depth profile for room temperature NF_3/Ar plasma exposed at room temperature bare aluminum alloy 5352 sample.

The anodized/sealed alloy 6061 sample (figure 4.18) had high levels of fluorine incorporated over 600 Å before dropping below 10 % following a room temperature NF_3/Ar plasma exposure. The oxygen concentration never regained the original value of 55% only rising to 50 % about 575 Å from the surface. The aluminum concentration achieved a level of 35% after only 200 Å as a result of fluorine incorporation in the anodization layer.

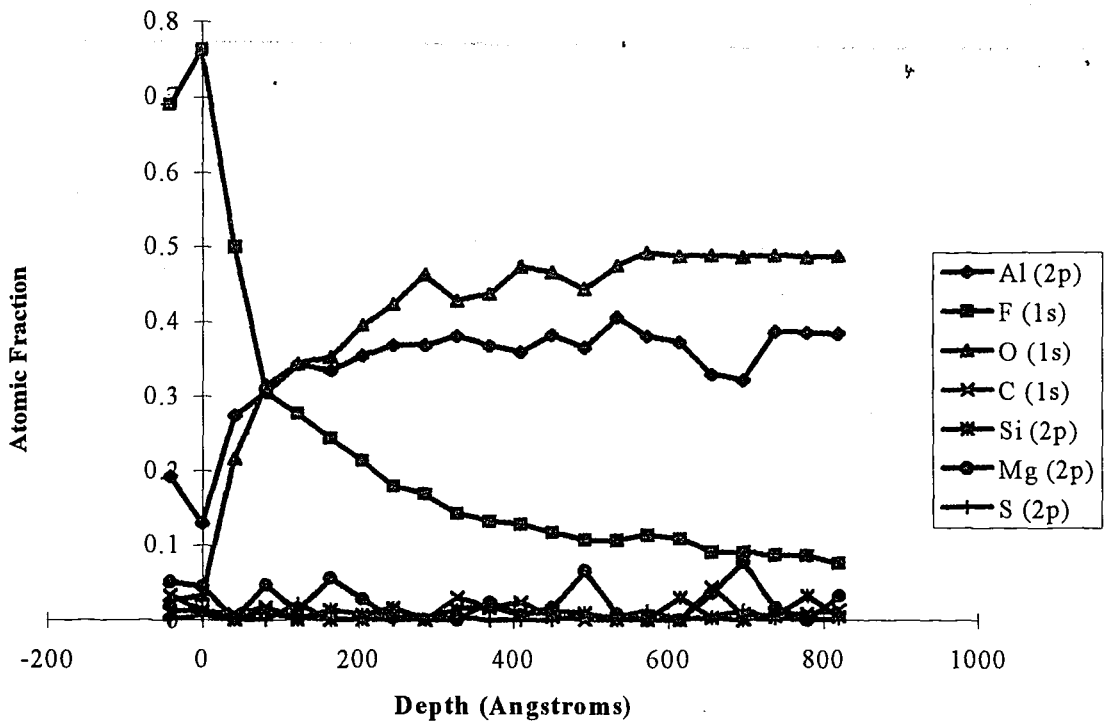

Figure 4.18: XPS depth profile of an NF_3/Ar plasma exposed at room temperature aluminum alloy 6061 anodized/sealed sample.

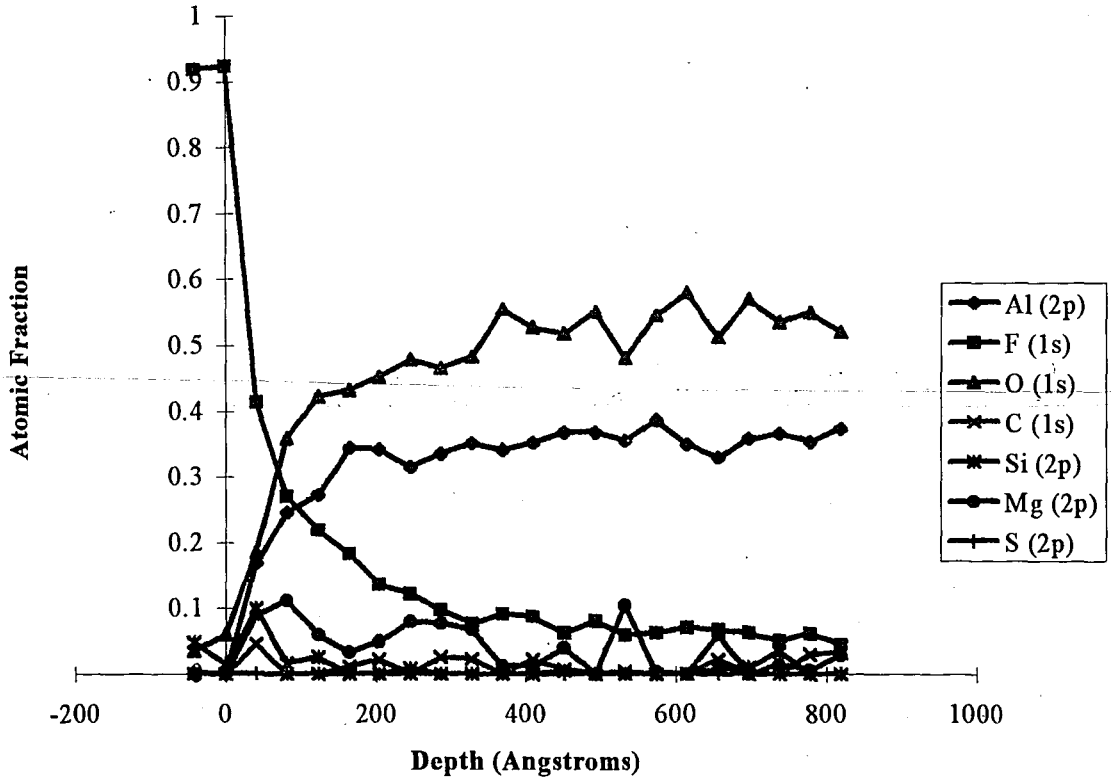

Figure 4.19: XPS depth profile of an NF3/Ar plasma exposed at room temperature aluminum alloy 5352 anodized/sealed sample.

The room temperature plasma exposed anodized/sealed 5352 alloy (figure 4.19), like the bare sample, had very high initial values of surface fluorine (over 90 %). However, the fluorine concentration for the anodized/sealed sample dropped more rapidly than the bare sample. Fluorine concentration dropped below 50 % in less than 50 Å and below 10 % in about 275 Å. The resulting oxygen and fluorine concentrations were roughly 50 % and 35 %, respectively. In contrast to the 6061 samples, the oxygen concentration returned to its pre-exposed value and the aluminum concentration decreased after exposure. Also, the magnesium concentration seemed to rise just as there was a sharp drop off in fluorine concentration, in about 200 Å, followed by a region starting about 400 Å, of magnesium depletion.

Two anodized/unsealed samples of each alloy were plasma exposed at different substrate temperatures, room temperature and 450 C. The alloy 6061 room temperature plasma exposed anodized/unsealed sample (figure 4.20) exhibited much better resistance to fluorine incorporation than the previous samples discussed. The fluorine concentration dropped to 10 % after only 125 Å, a significant improvement. Oxygen depletion was seen, but the oxygen concentration reached a maximum value of 45% after only 75 Å. The fluorine concentration, after sputtering into the surface over 800 Å, maintained its 10% value. One explanation is that the fluorine was driven deeper during sputtering or "knocked on" by the Ar^+ beam. Although these mechanisms may have contributed to the fluorine signal, the majority of the signal was attributed to fluorine freely diffusing down the pores of the anodized layer toward the base metal which will likely lead to rapid failure.

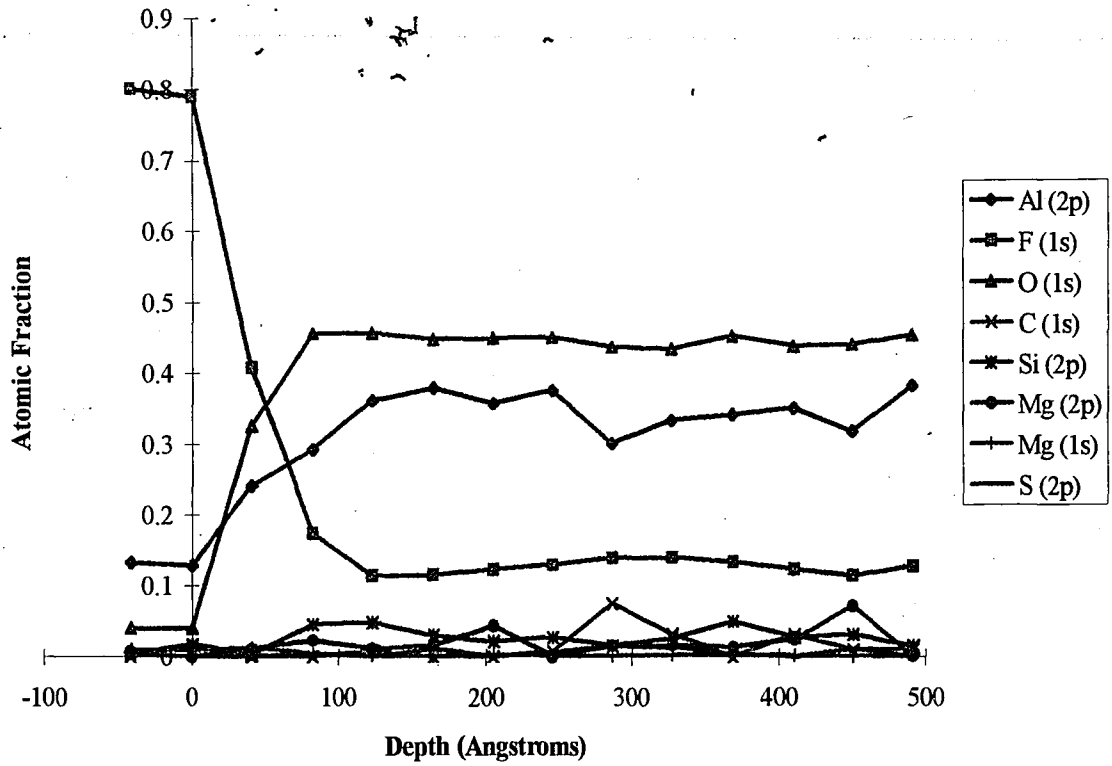

Figure 4.20: XPS depth profile of an NF_3/Ar plasma exposed at room temperature aluminum alloy 6061 anodized/unsealed sample.

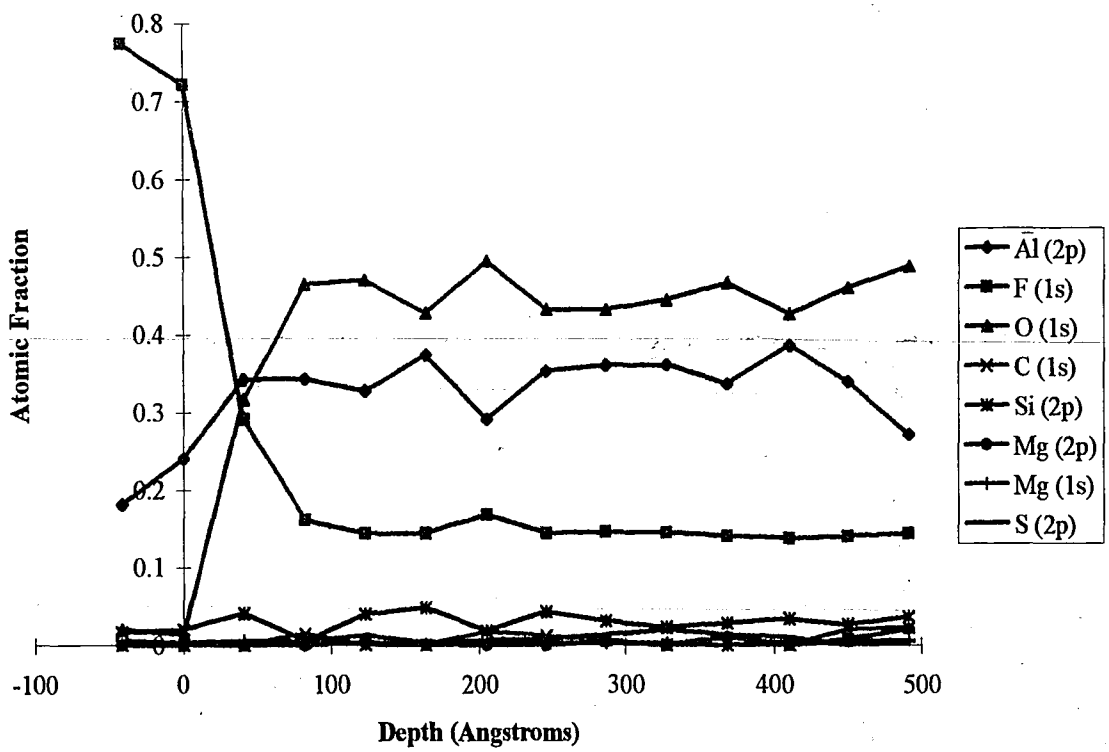

Figure 4.21: XPS depth profile of an NF_3/Ar plasma exposed at 450 C aluminum alloy 6061 anodized/unsealed sample.

Sealed anodized layers are supposed to give higher corrosion resistance then an unsealed surface. Based on the chemistry likely occurring in the pores, the hydroxyl groups in the hydrated aluminum oxide will be more reactive with fluorine than the anhydrous oxide.[40] The difference in reactivity may account for the increased fluorine concentration deeper into the anodized/ sealed layer. Also, the diffusion pathways of the hydrated aluminum oxide will be larger than those of the anhydrous oxide due to the inclusion of water molecules. Fluorine diffusing into the sealed surface can react with the hydroxyl groups or diffuse further inward. In either case, when the fluorinated environment is removed, the fluorine is "trapped" in the sealed oxide bulk layer. In the case of the unsealed anodized layers, when the fluorinated environment is removed, any unreacted fluorine in the pores will also be removed. Instead of increasing corrosion resistance, the end result for PECVD chamber cleaning applications is significantly poorer resistance.

The elevated temperature exposure of the alloy 6061 anodized/unsealed sample (figure 4.21) exhibited similar trends as the room temperature anodized/unsealed sample, but the fluorine level only decreased to 15%. This is consistent with the mechanism of the elevated temperature supplying additional energy for reactions to take place.

XPS analysis of the anodized/unsealed alloy 5352 sample following room temperature plasma exposure can be seen in figure 4.22. The initial surface fluorine concentration was about 70 % and dropped quickly below 50% in less than 50 Å. It dropped below 10 % in about 60 Å from the surface. The same phenomena as the anodized/sealed 5352 samples were seen; the oxygen concentration returned to its pre-

exposure value and the aluminum concentration reached a maximum of roughly 30 %. The magnesium concentration exhibited a series of enrichment and depletion regions starting at about 50 Å from the surface. The high temperature exposure of the anodized/ unsealed sample (figure 4.23) exhibited similar behavior.

Wernick[11] states that 5000 series aluminum alloys, which have higher magnesium concentrations, realize smaller weight gains for dry oxidation processes than the high purity aluminum metal. This is attributed to the presence of magnesium, which during the anodization process, becomes preferentially incorporated into the oxide layer, even at magnesium bulk levels of 50 ppm. Magnesium enrichment of the anodization layer creates

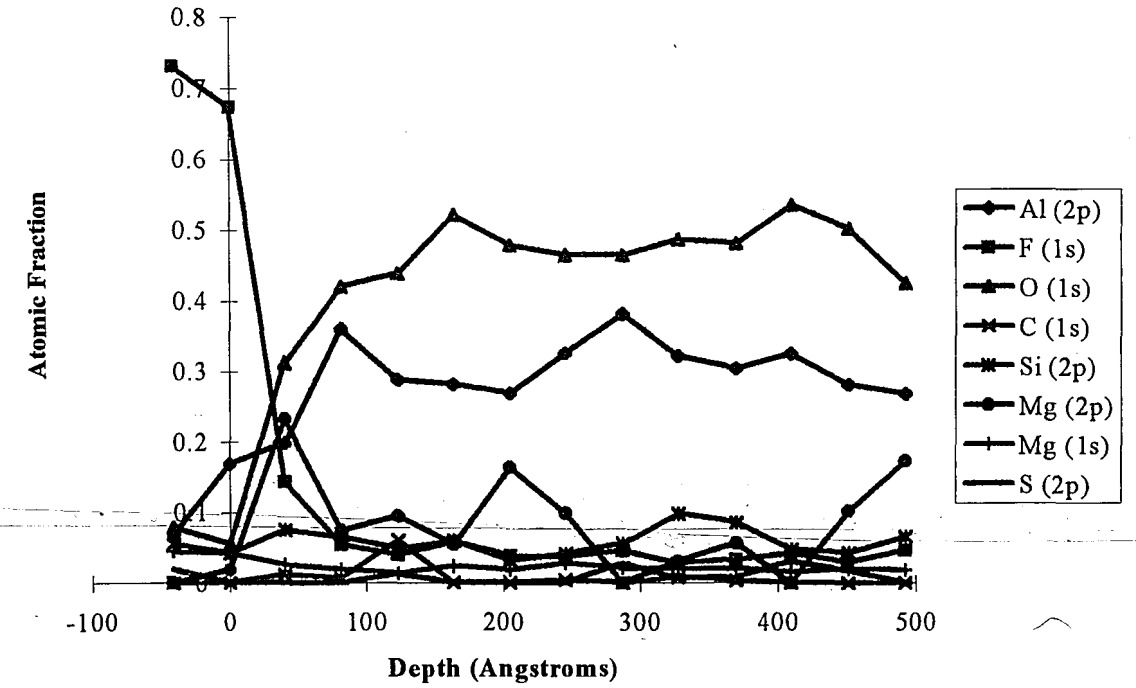

Figure 4.22: XPS depth profile of an NF_3/Ar plasma exposed at room temperature aluminum alloy 5352 anodized/unsealed sample.

a competitive oxidation reaction between the magnesium diffusing outward and the oxidant (Ox) diffusing inward. At levels up to 4 % magnesium, a duplex film of Al_2O_3

enrichment closer to the base metal and MgOx enrichment closer to the surface. This phenomena continues until the base alloy magnesium is depleted.

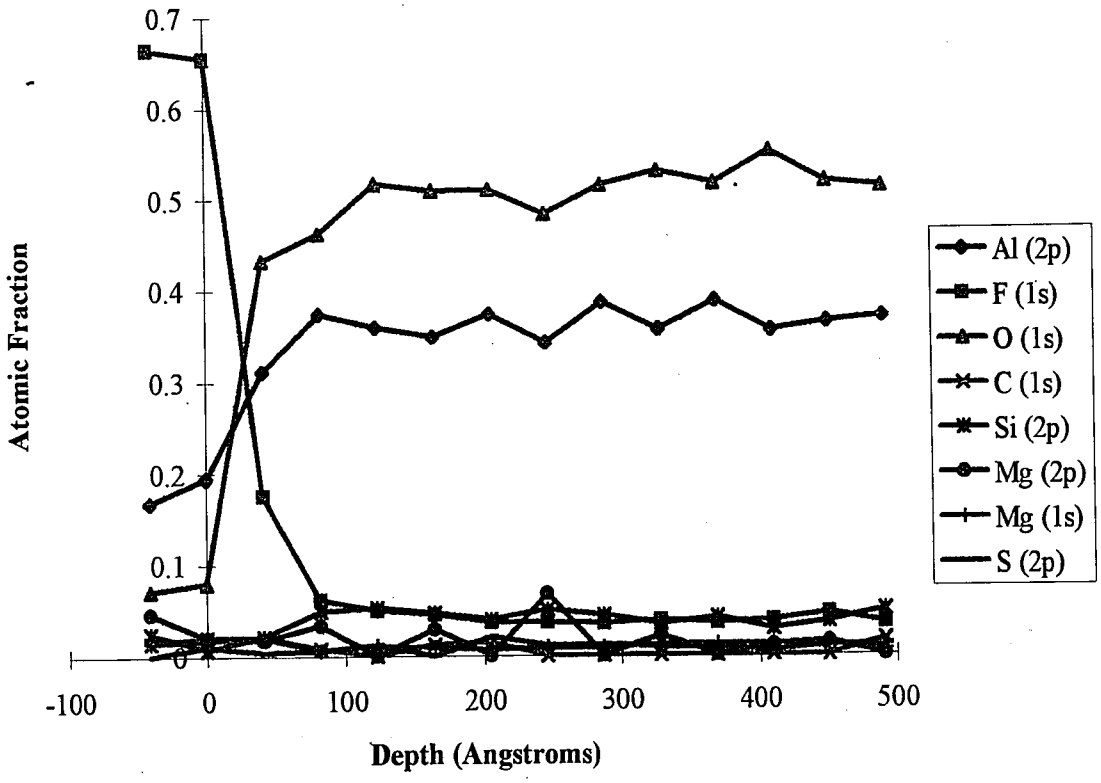

Figure 4.23: XPS depth profile of an NF_3/Ar plasma exposed at 450 C aluminum alloy 5352 anodized/unsealed sample.

It has been speculated in other work that during fluorine plasma exposure, formation of a protective layer of $AlMg_xF_y$ acts as a barrier to fluorine diffusion, thereby limiting the amount of fluorine incorporation in the anodization layer.[33] Breakdown of the oxide layer occurs from physiochemical attack by the anions, in this case fluorine. The anodization layers are not perfect crystalline structures, they are amorphous and have built in flaws which can act as nucleation sites for corrosion. Flaws are continuously being formed and healed, aggressive anions hinder the healing process, and can allow corrosion to propagate.

4.5 SUMMARY OF RESULTS

In summary, alloy 6061 seems to have the most corrosion resistance when the anodization layer was not sealed at lower temperatures. Since the temperatures seen in PECVD processes are elevated to 450 C, these results indicate that if alloy 6061 must be used, anodize the surface and do not seal the surface as the pore filler, hydrated aluminum oxide, provides a more reactive pathway towards the base metal than the anhydrous aluminum oxide. In all the alloy 6061 cases, the initial surface concentration of fluorine after exposure was around 75 % and dropped below 50 % rapidly, within 50 Å of the surface, with the exception of the bare surface where it didn't drop below 50% until about 250 Å were removed.

Alloy 5352 was more corrosion resistant than alloy 6061 with all surface treatments, except a bare surface. Coupled with the smaller grain sizes of the rolled 6061 samples and the difference in alloying agents, bare alloy 6061 seemed to fluorinate at a slower rate than the bare alloy 5352. As a result of the anodization process, magnesium diffuses preferentially into the oxide layer. Since there was no appreciable oxide layer on the bare sample surface, the magnesium concentration was comparably lower near the surface. The chemical potential gradient created by the fluorine plasma may not be large enough to pull the magnesium out, therefore an insufficient or no protective barrier was formed. Paramount to exhibiting good corrosion resistance is anodizing the surfaces leaving the pores unsealed. If these results can be extrapolated, using alloy 5352 instead of alloy 6061 will increase the lifetime of the plasma immersed parts.

A clear illustration of this is to plot the ratio of atomic fluorine concentration to atomic oxygen concentration as a function of depth into the surface for each alloy and surface treatment (figure 4.24). Since the bare samples do not exhibit "good" corrosion properties and the fact that they have no appreciable oxygen, they will not be displayed. Each surface treatment is displayed in the same color to illustrate the differences between the alloys. Sealed samples have larger overall ratios and do not inhibit fluorine incorporation very well as compared to the unsealed samples. Alloy 6061 unsealed samples exhibit similar characteristics with better fluorine corrosion resistance at both room temperature and 450 C than the sealed alloys. The alloy 5352 samples exhibit the best resistance toward fluorine corrosion; the initial ratios are a factor of two lower than the alloy 6061 samples and they maintain the advantage well into the surface.

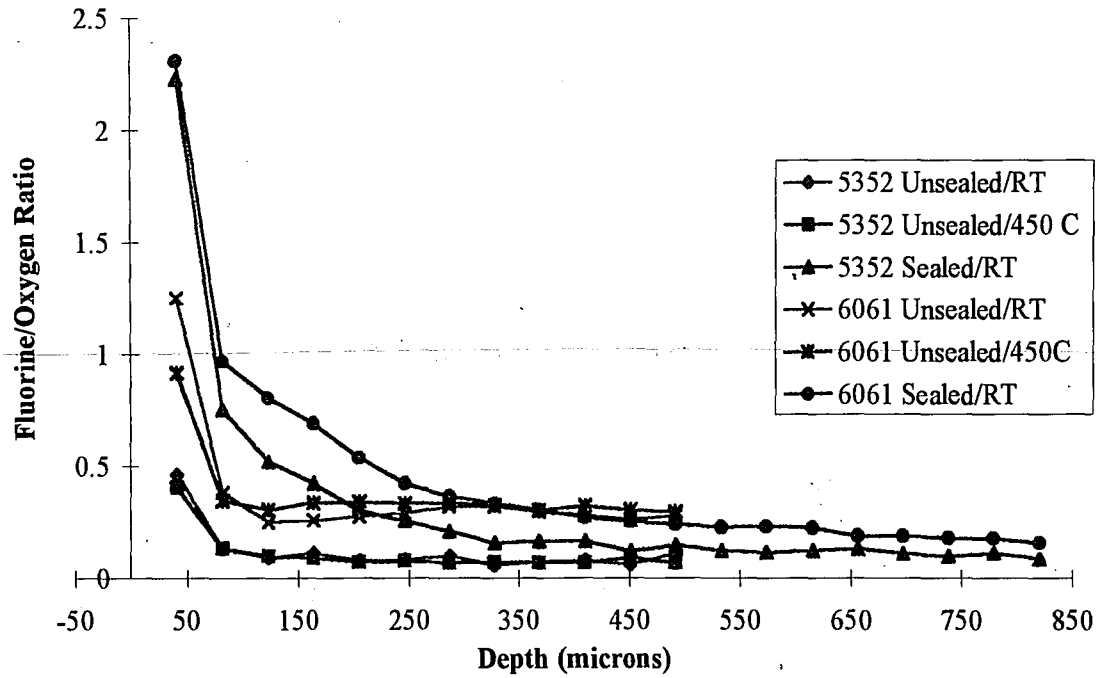

Figure 4.24: Fluorine/Oxygen ratio as a function of depth for each exposed anodized sample. (RT ≡ room temperature)

This plot shows that the anodized/sealed layers have higher initial fluorine incorporation, but farther into the layer they exhibit lower fluorine/oxygen ratios. This can be attributed to the fact that the plasma exposures were only one hour in length and fluorine incorporation into these layers is somewhat diffusion limited. If longer exposures were experienced, it can be speculated that the high initial levels of fluorine would be seen deeper into the anodized layer.

There was no attempt made in this work to measure corrosion rates or to determine the activation energy, if any, that must be overcome to initiate the corrosion. Listed in table 3 are some possible half reactions that may play a role in the surface corrosion reactions. This list does not include reactions that are proceeding in the bulk plasma, nor is it meant to be exhaustive, but rather includes only a few of the half reactions that may occur if the species are present at the surface of the anodization layer. The key is to have at least 2-4 % magnesium at the surface to form the protective diffusion barrier and stop fluorine incorporation at the surface.

Half Reaction	E° vs. Standard Hydrogen Electrode
$Al^{3+} + 3\ e^- \Leftrightarrow Al$	-1.662
$F_2 + 2\ H^+ + 2\ e^- \Leftrightarrow 2\ HF$	3.053
$F_2 + 2\ e^- \Leftrightarrow 2\ F^-$	2.866
$2\ H_2O + 2\ e^- \Leftrightarrow 2\ OH^- + H_2$	-0.828
$Mg^{2+} + 2\ e^- \Leftrightarrow Mg$	-2.372

Table 3: Possible half reactions that may contribute to the corrosion mechanism.[8]

4.6 SUGGESTIONS FOR FURTHER RESEARCH

This study did not include experiments investigating the effects of ion bombardment, possible etch rate of the materials, or the effects of more or less magnesium in the aluminum alloy. Experiments that investigate the effects of ion bombardment would require specialized equipment, but would give an idea of the additional surface energy that is available due to bombardment. By varying a 60 Hz biasing voltage to the lower electrode, kinetic information can be gained and could lead to a better understanding of this type of ion-assisted corrosion.

Measuring the etch rate of the substrate materials would also require very sensitive and specialized equipment, but the investment would determine whether these materials are being eroded as well as corroded during corrosive plasma processes. Perhaps a material exhibits good corrosion properties because the surface is continually being removed, thereby using the corrosive specie in the removal reaction rather than allowing it to diffuse into the protective layer or surface.

Varying the amount of alloying agents which are thought to enhance a materials corrosion properties to determine if more or less is better would require the utmost understanding and commitment from a manufacturer. Finally, using these optimal amounts of alloying agents, it may be possible to determine some of the reactions that are important for initiating fluorine corrosion, and therefore learn which ones to avoid. Finding the optimal amount of alloying agent could in the long term reduce materials costs, but increase the cost of ownership associated with the equipment using the material.

5.0 CONCLUSIONS

This work has demonstrated that careful choice of the alloying agents in aluminum can lead to significantly better corrosion resistance to fluorinated gas ambients. The key to these enhanced properties appear to be the magnesium enrichment zones which apparently form a protective diffusion barrier for the fluorine.

One important fact to keep in mind while considering the relevance of these data to semiconductor manufacturing is that these material exposures were *only* one hour in length. Even so, the extent of fluorination seen is impressive. In general, for each hour a PECVD production tool is in use, it is estimated that one-third of the time is spent cleaning the reactor. Advanced corrosion of the anodized aluminum parts occurs as a result of rapid exposure to the aggressive cleaning environments. If an anodized aluminum alloy 5352 part is used, instead of the standard alloy 6061, reduced corrosion is expected resulting in additional production time. Less time will be spent maintaining the tool and more time spent processing wafers.

The IC industry, like many other industries, strives to reduce the additional expenses created by corrosion. Choosing better alloys or alternative materials for use in this application can yield long term benefits. In addition to choosing the proper materials, it is also important to optimize the cleaning process so that exposure to aggressive fluorinated plasmas can be minimized, thus lengthening the lifetime of the parts.

REFERENCES

1. *Semiconductor Materials and Process Technology Handbook for very large sacle integration (VLSI) and ultra large scale integration (ULSI)*, edited by G. E. McGuire, (Noyes, New Jersey, 1988).

2. *Microelectronics Processing: Chemical Engineering Aspects*, edited by D. W. Hess and K. F. Jenson, (American Chemical Society, Washington DC, 1989).

3. Anner, G. E., *Planar Processing Primer* (Van Nostrand Reinhold, New York, 1990).

4. Mayer, J. W., Lau, S. S., *Electronic Materials Science: For Integrated Circuits in Si and GaAs,* (McMillian, New York, 1990).

5. Wolf, S., Tauber, R. N., *Silicon Processing for the VLSI Era Volume 1- Process Technology*, (Lattice, California, 1986).

6. Langan, J. G., Maroulis, P. J., Ridgeway, R. G., "Strategies for greenhouse gas reduction", Solid State Technology, **39** (7), 1996, p. 115-122.

7. Langan, J.G., Beck, S.E., Felker, B.S. Rynders, S.W., "The role of diluents in electronegative fluorinated gas discharges." J. Appl. Phys. **79** (8), 3886 (1996).

8. *Handbook of Chemistry and Physics*, edited by R. C. Weast (Chemical Rubber, Boca Raton, FL, 1986), F-186.

9. Hargis, P. J., Greenberg, K. E., Miller, P. A., Gerardo, J. B., Torczynski, J. R., Riley, R. E., Hebner, G. A., Roberts, J. R., Olthoff, J. K., Whetstone, J. R., Van Brunt, R. J., Sobolewski, M. A., Anderson, H. M., Splichal, M. P., Mock, J. L., Bletzinger, P., Garscadden, A., Gottscho, R. A., Selwyn, G., Dalvie, M., Heidenreich, J. E., Butterbaugh, J. W., Brake, M. L., Passow, M. L., Pender, J., Lujan, A., Elta, M. E., Graves, D. B., Sawin, H. H., Kushner, M. J., Verdeyen, J. T., Horwath, R., and Turner, T. R. Rev. Sci. Inst. **65**, 140 (1994).

10. Wada, K., Shimohira, T., Yamada, M., Baba, N., "Microstructure of porous anodic films on aluminum", J. Mat. Sci., **21**, 3810-3816 (1986).

11. Wernick, S., Pinner, R., Sheasby, P. G. *The Surface Treatment and Finishing of Aluminum and Its Alloys*, 5th ed, Vol. 1 and 2.

12. Strohmeier, B. R. "Evaluation of anodic Al_2O_3 barrier films for calibrating Auger sputter depth profiles". Forschung, **67**, 1209 (1991).

REFERENCES (con't)

13. Wagner, C. D., Riggs, W.M., Davis, L. E., Moulder, J. F., Muilenberg, G. E.(editor). *Handbook of X-Ray Photoelectron Scpectroscopy* (Perkin-Elmer Corp., Minn., 1979).

14. Bastin, G. F., Heijligers, H. J. M. "Nonconductive specimens in the electron probe microanalyzer-A hitherto poorly discussed problem." Electron Probe Quant. Edited by K. F. L. Heinrich and D.E. Newbury (Plenum Press, New York, 1991), 163.

15. Pliny. *Natural history of the world* (Heinemann, London, 1938).

16. Williams, A. R., "The knight and the blast furnace", Metals and Materials **2**, p. 485-489, (1986).

17. Trethewey, K. R., Chamberlain, J. *Corrosion for Science and Engineering*, 2nd ed.

18. Richards, J. W., Trans. Am. Electrochem. Soc. **1**, p. 1, (1902).

19. Whitney, W. R., "The corrosion of iron", J. Am. Chem. Soc. **25**, p 325 (1903).

20. Walker, W. H., "The function of oxygen in corrosion of metals", Trans. Am. Electrochem. Soc. **14**, 175-187, (1908).

21. Williams, "Influence of copper in retarding corrosion of soft steel and wrought iron", Iron Age **66**, 16, (1900).

22. Buck, D. M., "A review of the development of copper steel", Trans. Am. Iron and Steel Inst. P. 373-379, (1920).

23. Speller, F. N., *Corrosion Causes and Prevention* (McGraw-Hill, NY, 2 ed., 1935).

24. McKee, A. B., Brown, R. H., "Resistance of aluminum to corrosion in solutions containing various anions and cations", Corrosion **3** (12), p. 595-612, (1947).

25. Aziz, P. M., Godard, H. P., *ibid* **10**, p. 269, (1954).

26. Hubner, W., Wranglen, G., Scandinavian Corrosion Conference, Helsinki (1964).

27. Beard, F. M., Hine, K. A., "The effects of alloying constituents in aluminum on the corrosion attack by mercury", Brit. J. Corrosion **1**, p. 98, (1965).

28. Olden, M. J. F., Cameron, K. W. N., "Corrosion in the gas industry - the contemporary scene", Brit. J. Corrosion **3**, p. 271, (1968).

REFREFENCES (con't)

29. Vincent, L. M. "Corrosion by fluorinating agents". B.I.S.T. Commisariat de l'energie atomique, **161**, 17 (1971).

30. Vincent, L. M., Gillardeau, J., Hasson, R., Maraval, S. "Corrosion in a fluorinating environment - I. Behavior and choice of materials". Energie nucleaire. **11** (7), 400 (1969).

31. Vincent, L. M., Gillardeau, J., Hasson, R., Maraval, S. "Corrosion in a fluorinating environment - II. Study methods". Energie nucleaire. **11** (7), 411 (1969).

32. Langan, J. G., Felker, B. S., "Studies of the reaction of NF3/Ar and C2F6/O2 plasmas with anodized aluminum surfaces using x-ray photoelectron spectroscopy", Proc. Electrochem. Soc. Symp. Plasma Processing, **92-18**, p. 135, (1992).

33. Ponnekanti, S., Murugesh, L., Hanson, E. "Failure mechanisms of anodized aluminum parts used in chemical vapor deposition chambers". J. Vac. Sci. Technol. A. **14** (3), 1127 (1996).

34. Jones, D. A. *Principles and Prevention of Corrosion.* (Prentice-Hall, New Jersey, 1996).

35. Lucas, K. A., Clarke, H. *Corrosion of Aluminum-Based Metal Matrix Composites* (Research Studios Press, Inc, Somerset, England, 1993).

36. Fiaud, C., Vincent, L. "Resistance of alloys to halogens at high temperatures". Oberflaeche-Surf, 23 (7), 230 (1982).

37. Pruette, L. C., Karecki, S. M., Reif, L. R., Langan, J. G., Rogers, S. A., Felker, B. S., Ciotti, R. J. "Evaluation of trifluoroacetic anhydride as an alternative PECVD chamber clean chemistry". Submitted to J. Vac. Sci. Technol.

38. Communication with Ed Gradde of Alcoa.

39. Bhattacharya, A. K., Pyke, D. R., Reynolds, R., Walker, G. S., Werrett, C. R., "The use of O 1s charge referencing for the x-ray photoelectron spectroscopy of Al/Si, Al/Ti, and Al/Zr mixed oxides", J. Mat. Sci. Letters **16**, p. 1-3, (1997).

40. Miller, A. C., McClusky, F. P., Taylor, J. A., "An x-ray photoelectron spectroscopy study of aluminum surfaces treated with fluorocarbon plasmas", J. Vac. Sci. Technol. A, **9** (3), p 1461-1465, (1991).

VITA

Brian Scott Felker was born July 15, 1965 in Abington, Pennsylvania. He graduated with a Bachelor of Science in Physics from the Pennsylvania State University in January, 1990. Upon graduation he took a position as a research technician with the Atlas Powder Company working on a multi-component explosive optimization program. His tasks included making and testing the components for self life, temperature effects, and rate of detonation. At the conclusion of the contract, in 1991, he accepted a research technician position in the Electronics Research and Development group with Air Products and Chemicals, Inc.

At Air Products, where he is still employed, he became familiar with ultra high vacuum technology, equipment and related processes. He has designed and integrated several systems into a unique research apparatus. His research projects have included process optimization of nitrogen trifluoride PECVD chamber cleaning, fundamental electrical characterization of fluorinated plasmas, chemical vapor cleaning, and material compatibility with halogenated specie environments. He is the co-inventor on one patent and has co-authored over twenty papers. In 1993, he enrolled at Lehigh University in the Materials Science and Engineering Department.

END OF TITLE